Article



Inferring diffusion, reaction, and exchange parameters from imperfect FRAP

Enrico Lorenzetti, ^{1,2} Celia Municio-Diaz, ^{3,4} Nicolas Minc, ^{3,4} Arezki Boudaoud, ^{1,*} and Antoine Fruleux^{2,*} ¹Ladhyx, CNRS, Ecole Polytechnique, Institut Polytechnique de Paris, Palaiseau, France; ²LPTMS, CNRS, Université Paris-Saclay, Orsay, France; ³Université Paris Cité, CNRS, Institut Jacques Monod, Paris, France; and ⁴Equipe Labellisée LIGUE Contre le Cancer, Paris, France

ABSTRACT Fluorescence recovery after photobleaching (FRAP) is broadly used to investigate the dynamics of molecules in cells and tissues, notably to quantify diffusion coefficients. FRAP is based on the spatiotemporal imaging of fluorescent molecules after an initial bleaching of fluorescence in a region of the sample. Although a large number of methods have been developed to infer kinetic parameters from experiments, it is still a challenge to fully characterize molecular dynamics from noisy experiments in which diffusion is coupled to other molecular processes or in which the initial bleaching profile is not perfectly controlled. To address this challenge, we have developed HiFRAP to quantify the reaction- (or exchange-) diffusion kinetic parameters from FRAP under imperfect experimental conditions. HiFRAP is based on a low-rank approximation of a kernel related to the model Green's function and is implemented as an ImageJ/Python macro for (potentially curved) one-dimensional systems and for two-dimensional systems. To the best of our knowledge, HiFRAP offers features that have not been combined together: making no assumption on the initial bleaching profile, which does not need to be known; accounting for the limitation of the optical setup by diffraction; inferring several kinetic parameters from a single experiment; providing errors on parameter estimation; and testing model goodness. In the future, our approach could be applied to other dynamical processes described by linear partial differential equations, which could be useful beyond FRAP, in experiments where the concentration fields are monitored over space and time.

SIGNIFICANCE Fluorescence recovery after photobleaching (FRAP) is a microscopy approach that is widely used to investigate the diffusion and transport of molecules in life sciences and in material sciences. Numerous methods have been developed to derive kinetic parameters such as diffusion and binding coefficients. However, these methods suffer from limitations associated with experimental constraints, such as technical noise or an imperfectly known initial condition. To circumvent these limitations, we developed a comprehensive approach to estimate several kinetic parameters from a single experiment, to assess the precision of estimation, and to test whether the underlying model is well suited. We implemented this approach in HiFRAP, an ImageJ/Python macro of broad applicability to one- and two-dimensional systems.

INTRODUCTION

Cells and tissues are the place of permanent transport and transformation of matter. At cellular level, trafficking, binding and unbinding, or diffusion, are essential in the self-organization of the cell, for instance. At multicellular level, diffusion, directed transport, and degradation of morphogens are key to setting morphogen distributions and providing positional information during organism develop-

ment. Several methods have been developed to assess such molecular dynamics, including fluorescence recovery after photobleaching (FRAP), fluorescence spectroscopy, or single-particle tracking (1). Among these, FRAP appears as the most widely used method (1–5), likely because the microscopy setup is technically accessible.

FRAP is designed to study the dynamics of fluorescent molecules by monitoring the response to an initial perturbation. Molecules are first photobleached by strong and short light pulses in a region of the sample, a spot that is often disk or square shaped. This causes a drop in light intensity reemitted by the sample in this region. Fluorescence is then followed over space and time by time-lapse imaging with a microscope. Typically, the fluorescence (partially) recovers

Submitted May 5, 2025, and accepted for publication July 30, 2025.

*Correspondence: arezki.boudaoud@polytechnique.edu or antoine. fruleux@cnrs.fr

Editor: Sudipta Maiti.

https://doi.org/10.1016/j.bpj.2025.07.036

© 2025 Biophysical Society. Published by Elsevier Inc.

All rights are reserved, including those for text and data mining, AI training, and similar technologies.



its initial level, and the pattern of recovery is informative of the underlying dynamics. Different bleaching geometries have been used depending on the biological system under investigation, imaging speed, and optical resolution. As alternative to spot FRAP (e.g., bleaching a disk), a long and thin strip can be bleached (6,7) and a line orthogonal to the strip is monitored, allowing for a faster imaging rate and a simplified analysis using one-dimensional (1D) spatial models. Another configuration is inverse FRAP (iFRAP), where the entire system is bleached except for a small region (8). Inverse FRAP can also be implemented using photoconversion, rather than traditional photobleaching, to reduce photodamage and better preserve cell viability during imaging (9). In this setup, the fluorescent signal is present only in a specific region first and then decreases over time, yielding a decay curve.

FRAP is routinely used to determine diffusion coefficients. When molecules only undergo diffusion, the timescale of fluorescence recovery (or decay for iFRAP) is a function of the diffusion coefficient and of the size and shape of the initially bleached region (we will often use FRAPped region in the following) (3–5). When molecules only undergo binding and unbinding to immobile substrates, then the timescale of fluorescence recovery is the inverse of the binding rate (3-5). Here, we consider more complex situations where several molecular processes are coupled, such as diffusion and binding/unbinding.

At the cellular level, FRAP has also been used to investigate protein synthesis (10), dynamics of molecular condensates (11), mechanosensing (12), transport of mRNA (13), or cell adhesion (14,15). At the tissue level, FRAP has been used to assess diffusion of morphogens (16) or expansion of the extracellular matrix (17). FRAP also appears in material science, for instance, to characterize pharmaceutical compounds (3,18). Despite the practical importance of FRAP, a comprehensive method to analyze and interpret FRAP data is still lacking (3). Here, we contribute to tackling this issue.

The classical method to determine diffusion coefficient is based on the theoretical calculation of the average concentration in the bleached region and fits to the recovery curve of fluorescence in that region (19,20). Although the classical method is easy to implement, it assumes that the initial bleaching profile is perfectly known, it does not use the information available in spatial variations, and it does not easily allow to distinguish diffusion from other processes (19). These limitations prompted the development of more sophisticated methods. Methods that do not require the knowledge of the bleaching profile are based on the decomposition of the fluorescence levels into Fourier modes and fit the temporal decay of the mode amplitude to theoretical solutions, in linear (21,22), in axisymmetric geometry (23), or without assumptions on geometry (24). Methods that use all spatial information to improve precision use fits of the spatiotemporal concentration field to analytical (25) or numerical (26,27) solutions of the diffusion equation, the former being restricted to Heaviside-like initial bleaching profile and the latter allowing initial bleaching profile of arbitrary shape. Other studies built methods to account for the effect of boundary conditions on diffusion (11), for diffusion on curved surfaces (9,28), or for anomalous diffusion (29,30).

Several studies have addressed the use of FRAP to determine the kinetic parameters of chemical reactions, binding/ unbinding dynamics, or exchanges between compartments, which all formally amount to chemical reactions. In general, these studies directly deduce constants from average prebleaching fluorescence and recovery time of average fluorescence in the bleached area (10,31-33), possibly accounting for rapid diffusion before the reactions take place. However, there are discrepancies between values of kinetic parameters according to the model used (34) and it is difficult to disentangle reactions from diffusion (35).

Another line of investigation has accounted for the coupling between reactions and diffusion. It is possible to solve numerically reaction-diffusion equations in complex realistic geometries to simulate FRAP and investigate changes in qualitative behavior according to parameters (36). To obtain kinetic parameters, an option is to use fluorescence recovery in the bleached area or in the region of interest (ROI) and to fit analytical recovery curves of several experiments with varying sizes of the bleached regions, which provides enough information to deduce more than one kinetic parameter (6,37,38). Another option is to use all spatial information and fit the spatiotemporal concentration field (fluorescence level) to analytical (29,39) or numerical (40–43) solutions of reaction-diffusion equations (for one or two species, according to the problem of interest). We note that these methods are constrained by the need to know the initial condition, i.e., the profile of fluorescence after initial bleaching. Using Fourier coefficients of the fluorescence field (44) like in some of the methods to infer diffusivity already mentioned, it was possible to get rid of this constraint, at the price of averaging several experiments together to average out noise. We aim at going beyond limitations by noise and the need to precisely know the bleached profile. Indeed, the bleached profile is difficult to control experimentally (24) and discrepancies with the assumed profile generally lead to a misestimation of kinetic parameters (6,20).

Some studies accounted for other couplings, such as advection (directed transport) and diffusion (19), advection-reaction (45), or advection-reaction-diffusion (13), with similar limitations to those previously discussed. Here, we only consider reaction-diffusion, but we note that our method is generalizable to any process described by linear partial differential equations (PDEs). In addition, we account for photobleaching during imaging, i.e., bleaching of fluorophores due to their excitation during time-lapse imaging, following a few studies that inferred the rate of photobleaching during imaging from experimental data (23,26,42).

Altogether, we aim at building a method to infer from FRAP the kinetic parameters of a process described by a reaction-diffusion equation from single experiments. We assume that experiments are noisy, that the initial bleaching profile is unknown, and that gradual photobleaching occurs due to imaging. We also account for the diffraction-limited resolution of the optical setup. We have named our approach HiFRAP, for highly informed FRAP, because we maximize the use of available spatiotemporal information. In the following, we formulate the problem as one of cost minimization and propose a systematic method to solve it. We validate and optimize the approach with synthetic data. Finally, we present HiFRAP, the implementation of the approach as an ImageJ macro (available at https:// github.com/lorenzetti1996/HiFRAP project), and illustrate it with experimental data on the transmembrane protein Mtl2p in fission yeast (46).

RESULTS AND DISCUSSION

General framework in the case of pure diffusion

FRAP experiments involve imaging at regular intervals a ROI containing the initially bleached (FRAPped) domain. The quantity of light emitted from the sample is proportional to the local concentration of fluorescent molecules, as long as saturation of the detectors is avoided. However, imaging the sample also results in photobleaching, so that fluorescence is attenuated by a constant factor after each image. The optical setup causes a spatial smoothing of the light pattern due to diffraction, which is characterized by the point-spread function of the microscope. The recorded signal results from three contributions. The first contribution is proportional to the concentration of fluorescent molecules, provided appropriate tuning of the excitation laser and detector gain; it contains a noisy part due to the statistical fluctuations of the number of these molecules in a small volume. The second contribution originates in technical noise, mostly associated with the detector. The third contribution is a background homogeneous signal associated with the detector. Accordingly, the recorded signal is a smoothed version of the field of fluorophore concentration, combined with noise and shifted by a background intensity. In HiFRAP, we account for point-spread function, photobleaching during imaging due to imaging, background intensity, and noise. The time-lapse data are assumed to be a temporal sequence of square images. The signal to be analyzed is sampled n_t times after every time interval Δt , over $n_x \times n_x$ square pixels of side length Δx .

For the sake of simplicity, we introduce and validate HiFRAP assuming that the underlying dynamics is set by diffusion only. We generalize our approach to reactiondiffusion in applying HiFRAP to reaction-diffusion. We illustrate our approach in two dimensions, although the ImageJ/Python plugin is also implemented for diffusion along a line. The concentration of fluorophores c(x, y, t) is a function of spatial coordinates (x, y) and of time t. It is a solution of the diffusion equation

$$\partial_t c = D_{\text{true}} \nabla^2 c, \tag{1}$$

where D_{true} is the true diffusion coefficient, ∂_t is the partial derivative with respect to time, and ∇^2 the Laplace operator. Our goal is to provide the best estimate D_{est} of the diffusion coefficient.

When photobleaching during imaging is not negligible, homogeneous regions of the sample (far from the FRAPped domain) show fluorescence decaying by a factor $\rho_i = \exp(-\varepsilon t_i/\Delta t)$, where ε is the decay rate per image, t_i the time at which the *i*-th image is collected, and Δt is the time interval between two consecutive images. The decay rate per image ε directly relates to the light dose received by the sample at each data acquisition. On many experimental setups, this quantity is fixed and does not depend on the time step Δt , which is our assumption throughout this article. In classical wide-field fluorescence microscopy, for example, most systems use a shuttered illumination setup in which the excitation light (e.g., from a mercury lamp) only reaches the sample during camera exposure. In confocal laser scanning microscopy or multiphoton microscopy, ε corresponds to the fluoresence decay induced by the light dose delivered during a single scan. The theoretical solution of the diffusion Eq. 1, $c(x, y, t_i)$ should be multiplied by this factor ρ_i . Photobleaching, however, does not affect the background intensity, I_{BG} , which is considered to be constant in time and space. The background value I_{BG} and the decay rate per image ε are either supposed to be known from regions distinct from the FRAPed area as explained in applying HiFRAP to experimental data, or inferred altogether with the dynamical parameters as discussed in applying HiFRAP to reaction-diffusion.

Fig. 1 A shows an example of the synthetic data set generated by solving analytically the diffusion Eq. 1. The ROI is a square of side length L. The FRAPped domain is a square of side length $\ell = L/3$ in which the fluorophores concentration is set to 0 at t = 0. The first row shows the simulated spatial profile of the fluorophore concentration, which becomes smoother and converges to the initial density over time, as could be expected. The second row shows a microscope-like time-lapse imaging, obtained from the simulated (true) concentration field by adding an uncorrelated Gaussian random variable corresponding to technical noise and applying a Gaussian spatial filtering corresponding to the point-spread function of the optical setup (see artificial data). In the following, we use such synthetic data to test our method and estimate the precision of the estimated diffusion coefficient, $D_{\rm est}$, with respect to its true value, D_{true} .

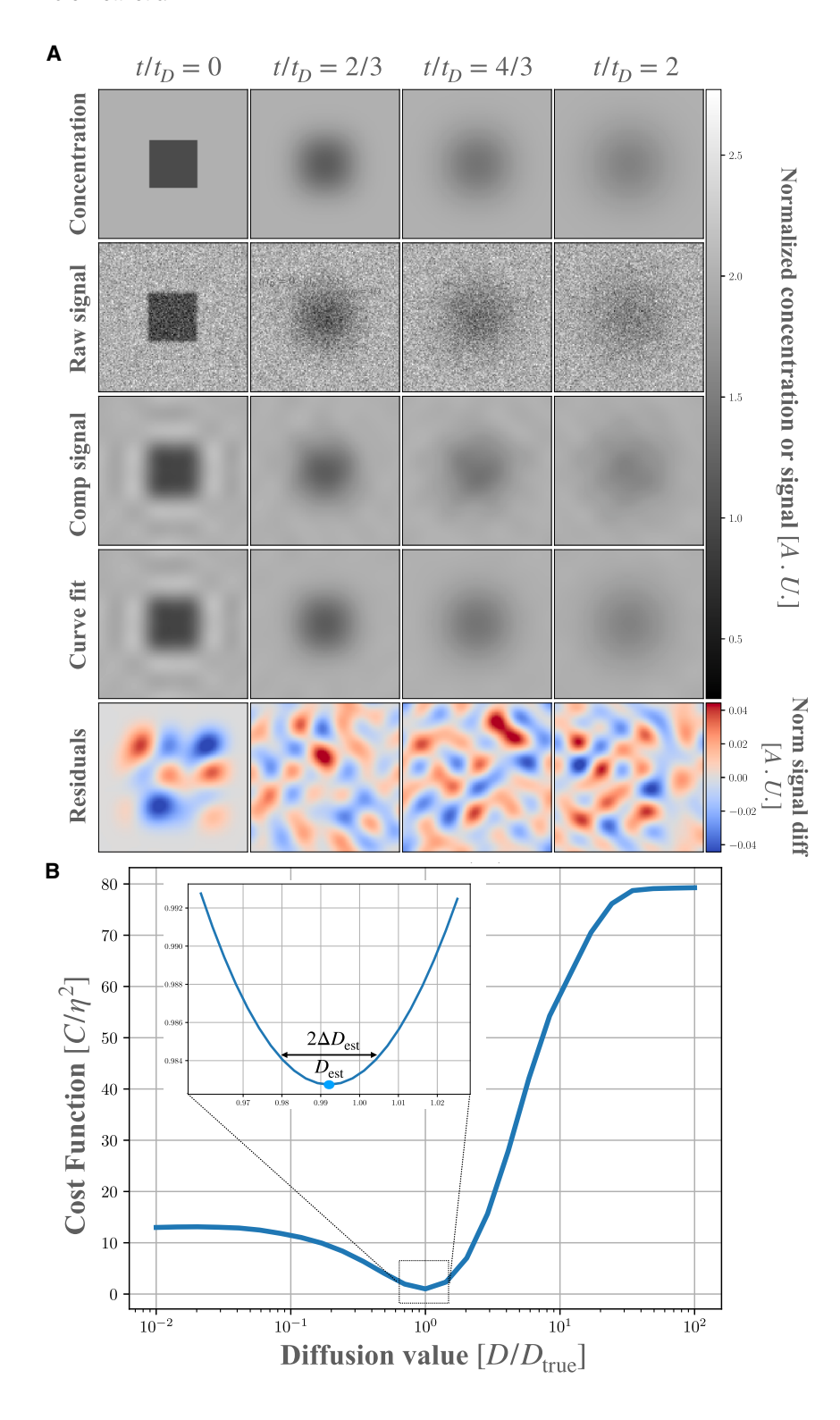


FIGURE 1 Inferring the diffusion coefficient from simulated FRAP. (A) A square region of interest of side length L is monitored and a central square region of side length $\ell = L/3$ is FRAPped at t = 0. From top to bottom: raw artificial data, microscope-like synthetic data accounting for diffraction and technical noise, compressed synthetic data, concentration field fitted by HiFRAP, and residuals of the fit. From left to right: snapshots from t = 0 to $t = 2t_D$, where $t_D = \frac{\ell^2}{16D_{\text{max}}}$ is taken as a unit of time. Gray- and colorscales indicate the concentration or signal intensity normalized by the drop in concentration ΔI at t = 0 in the FRAPped square. Dark (blue) to bright (red) indicate low to high concentration or signal. The decay rate per image due to photobleaching is set to $\varepsilon = 0$. For other parameters, default values are given in artificial data. (B) Cost function C (normalized by noise amplitude η) as a function of fitting diffusion coefficient D (normalized by its true value D_{true}), with a magnification of the neighborhood of the minimum of C in the inset. The cost function is minimal at $D_{\rm est}$, which is close to $D_{\rm true}$, up to an estimated error ΔD_{est} . The total observation time T for this data set is $T = 2t_D$ and the time step $\Delta t = 0.133t_D$.

A method to infer parameters from FRAP experiments

HiFRAP estimates kinetic parameters such as diffusion coefficient independently of any assumptions on the initial bleaching pattern. We use $N_{\text{tot}} = n_x \times n_x \times n_t$

(2D spatial × temporal) pixels from time-lapse imaging. We fit a theoretical model to those data by minimizing a cost function that quantifies the differences between observed data and theoretical solution. The model is built from the solution for (Eq. 1) and accounts for the point-spread function (see general framework in the case of pure

diffusion for more details). The estimated kinetic parameters are insensitive to the details of the point-spread function (29), provided its width μ exceeds the pixel size Δx , as shown in Fig. S4—a condition generally met in experiments. We therefore set $\mu = \Delta x$ by default and do not require experimental determination of the point-spread function.

The fit of the model to the data is performed iteratively in two steps, each minimizing the cost function: at each iteration, we first estimate the initial conditions for fixed kinetic parameters, and then update the kinetic parameters (in this case, the diffusion coefficient). To estimate the initial conditions, we use both spatial and temporal data and define the cost function as the sum of squared deviations between model predictions and the observed data. Because the PDE is linear with respect to the initial condition, the model response is also linear, and the cost function becomes quadratic in the initial condition. As a result, for fixed kinetic parameters, the optimal initial condition can be obtained by solving a linear system of equations. Once the cost is minimized with respect to the initial conditions (for fixed kinetic parameters), it is normalized by the effective number of degrees of freedom (see fitting model parameters). The kinetic parameters are then updated by minimizing the normalized cost using the reflective trust region algorithm (47), which is suited to bounded nonlinear least-squares problems.

Two important subtleties arise in the estimation of initial conditions at each iteration. First, the problem is inherently ill-posed: an infinite number of initial conditions can produce the same observed data, since measurements are finite while the initial condition is a continuous field belonging to an infinite-dimensional space. To address this, we use pseudoinversion to identify the components of the initial condition that influence the observed data. This reveals that only a limited number of degrees of freedom in the initial pattern significantly affect the measurements. Second, pseudoinversion becomes computationally expensive for large data sets, as it involves operations on matrices of size $N_{\text{tot}} \times N_{\text{tot}}$, which is prohibitive when $N_{\text{tot}} > 10^5$. To overcome this, we reduce the data size through compression, enabling implementation in an interactive ImageJ plugin. Specifically, we apply a discrete Fourier transform to compress the data in both spatial dimensions and retain only a subset of Fourier components. This reduces the data set to a manageable size $N = n_q \times n_q \times n_t$. As shown in optimizing experimental and analysis parameters, we find that values of n_q between 5 and 9 are sufficient to obtain reliable estimates of the kinetic parameters. The resulting compressed data set, with N on the order of 10^3 to 10^4 , allows efficient pseudoinversion to compute the optimal initial condition for the current estimate of the kinetic parameters (here the diffusion coefficient D).

To assess the uncertainty of the inferred parameter, we assume the cost around the minimum to be quadratic with

respect to the fitting parameter and we estimate the curvature of the cost function around the minimum by computing the Hessian as a higher curvature indicates higher precision (Fig. 1 B), see error on parameter estimation and goodness of the fit for details. To evaluate the goodness of the fit we use two metrics. The adjusted coefficient of determination $R_{\rm adi}^2$ is the classical coefficient of determination (R^2) corrected using the effective number of degrees of freedom; it quantifies how well the model explains variations of the observed data, and ranges from 0 (no explanation) to 1 (perfect fit). A limitation of the $R_{\rm adj}^2$ is that its value may depend on the amplitude of noise and on the initial bleaching profile (see error on parameter estimation and goodness of the fit). Accordingly, the $R_{\rm adi}^2$ should be used to compare two models applied to the same experiment, as used in applying HiFRAP to reaction-diffusion and applying HiFRAP to experimental data. The second metrics is not sensitive to the level of noise and the bleaching profile as it estimates whether the distribution of residuals is compatible with a Gaussian distribution using the Kolmogorov-Smirnov test. It returns a p value indicating whether to reject the null hypothesis that the residual distribution is compatible with a Gaussian. The only limitation is that it is computationally very slow because it involves an explicit calculation of all residuals in an appropriate basis, see error on parameter estimation and goodness of the fit.

HiFRAP is illustrated with synthetic data in Fig. 1. In (A), the two first rows are the true concentration of fluorophores and the simulated microscope-like images. For our analysis, we compress the microscope-like images (third row) to which we fit the model (fourth row), obtaining relatively small residuals (fifth row). In (B), we plot the cost function (after optimizing the initial condition) as a function of the fitting parameter D for the diffusion coefficient. The estimated diffusion coefficient D_{est} is defined as the value of D that minimizes the cost. We use the curvature of the cost function (inset in B) and noise amplitude to estimate the uncertainty $\Delta D_{\rm est}$ on the diffusion coefficient, see error on parameter estimation and goodness of the fit. Here, the coefficient of diffusion is well estimated, $D_{\rm est}/D_{\rm true} = 0.992$, and the relative uncertainty $\Delta D_{\rm est}/D_{\rm est}=0.01$ is small. Finally, we test the validity of the model by examining whether residuals are normally distributed, which is implemented using the Kolmogorov-Smirnov tests (48) (see error on parameter estimation and goodness of the fit). Here, we find a p value of 0.57, showing that the diffusion model is a good model for these data, as could be expected. Moreover, the adjusted coefficient of determination has a value $R_{\text{adi}}^2 = 0.989$, although it is only meaningful when comparing two models applied to a single data set.

HiFRAP was also implemented for FRAP experiment along a line. In Fig. S6, we show an example of HiFRAP inference applied to synthetic data for a 1D diffusive system, with similar results to the 2D case.

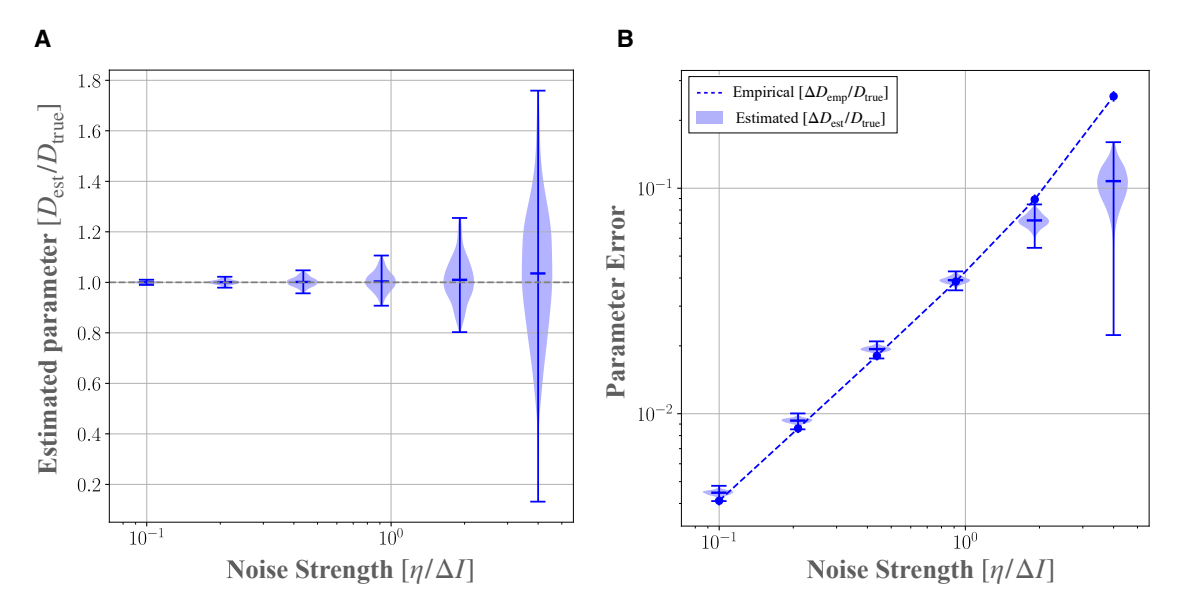


FIGURE 2 Validation of HiFRAP on a collection of synthetic data. (A) Estimated diffusion coefficient $D_{\rm est}$; B estimated uncertainty $\Delta D_{\rm est}$ and empirical error $\Delta D_{\rm emp}$. The quantities are all normalized by the true diffusion constant $D_{\rm true}$ and plotted as a function of the normalized noise amplitude $\eta/\Delta I$, where η is noise amplitude, ΔI is the drop-off in intensity after initial photobleaching. Violins represent distributions of $D_{\rm est}$ and $\Delta D_{\rm est}$ while the ticks highlight average and extreme values. The dashed gray line in (A) represents the reference value $D_{\rm est}/D_{\rm true}=1$, while the dashed blue line in (B) corresponds to the empirical error $\Delta D_{\rm emp}$. The number of realizations is 200 for each value of noise strength and the decay rate per image due to photobleaching is set to $\varepsilon=0$.

Validation on artificial data

To thoroughly evaluate the robustness of the inference method, we applied HiFRAP to six collections of synthetic data sets of size $n_{\rm ds}$, each corresponding to a different noise level. Within each collection, multiple data sets were generated using identical model parameters (as in Fig. 1) but with different realizations of the noise. For each synthetic data set, we estimated the diffusion coefficient $D_{\rm est}$ and its error $\Delta D_{\rm est}$. For each collection, we computed the average estimate $\langle D_{\rm est} \rangle$ (the brackets $\langle \ \rangle$ stand for average over the collection) and the empirical error $\Delta D_{\rm emp} = \sqrt{\frac{n_{\rm ds}}{n_{\rm ds}-1}} \langle (D_{\rm est}-D_{\rm true})^2 \rangle$.

In Fig. 2, we plotted the estimated diffusion coefficient $D_{\rm est}$ and estimated uncertainty $\Delta D_{\rm est}$ as a function of noise strength. Fig. 2 A shows that the distribution of D_{est} is well centered around its true value D_{true} . The standard deviation of this distribution increases with the noise amplitude η and the coefficient of variation $\Delta D_{\rm emp}/D_{\rm est}$ reaches values comparable with 1 for noise strengths η such that η / $\Delta I \sim 10^{-2} \sqrt{N_{\text{tot}}} \simeq 4$, where ΔI is the amplitude of the drop in intensity after initial photobleaching. Fig. 2 B shows that the estimated error $\Delta D_{\rm est}$ agrees well with the empirical error ΔD_{emp} , except for the highest amplitude of noise, validating the estimation of error from a single data set. HiFRAP also works for diffusion along a line as shown with synthetic data in Fig. S6, although with less precision due to less spatial averaging (less pixels) than in 2D diffusion. Overall, HiFRAP provides good estimates of the diffusion coefficient and of its error from a single experiment.

Optimizing experimental and analysis parameters

To optimize the estimates of kinetic parameters (here diffusion coefficient), we aim at tuning parameters that are accessible in experiments-side length of FRAPed region ℓ , number of time frames n_t , and delay between frames Δt —and in analysis—number of modes n_q kept for the compression. We implicitly assume the space resolution, Δx , to be constrained by the microscope used and the side length of the ROI, L, to be constrained by the size of the system and its spatial variations—the ROI should be as big as possible while sufficiently homogeneous. The bleaching size ℓ and the number of modes n_a influence the amount of useful spatial information. To be optimal, the size of the FRAPped region ℓ should be large enough for the perturbation in fluorescence associated with FRAP to be of significant weight compared with noise, whereas ℓ comparable with L leads to a loss of spatial information contained in the periphery of the FRAPped region. We found that the error on estimation of the diffusion coefficient is minimal roughly around $\ell \sim L/3$ in the case of a square FRAPped region. Concerning the number of modes kept in the discrete Fourier transform, fair estimates are reached for $n_q \ge 5$ (Fig. S2). Accordingly, we took $\ell = L/3$ and $n_q = 9$ in all our analyses, except when specified otherwise.

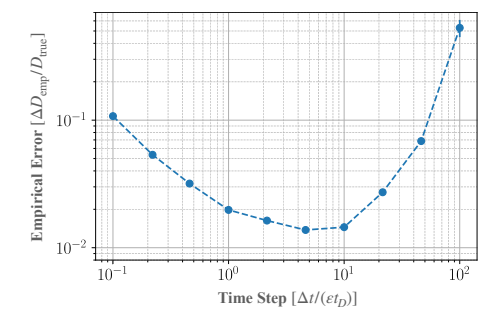


FIGURE 3 Optimization of imaging time step Δt . The empirical error $\Delta D_{\rm emp}$, normalized by the true diffusion coefficient $D_{\rm true}$, is represented as a function of relaxation time $\Delta t/\varepsilon$ due to photobleaching during imaging, normalized by the diffusive timescale $t_D = \ell^2/D_{\rm true}/16$. The empirical error was computed as $\Delta D_{\rm emp} = \sqrt{\frac{n_{\rm ds}}{n_{\rm ds}-1}}\langle (D_{\rm est}-D_{\rm true})^2\rangle$ from the estimated values $D_{\rm est}$ and true value $D_{\rm true}$ of the diffusion coefficient from $n_{\rm ds}=200$ artificial data sets. Error bars represent the estimated standard error of the empirical error.

The time resolution of experiments may be constrained by the sample imaged, for instance, when there is phototoxicity. Here, we only consider constraints due to the optical setup, which are mostly associated with photobleaching during imaging. The intensity of the observed signal decays with the number of images acquired, proportionally to $\exp \left[-\varepsilon (n_t-1)\right]$, so that the signal quickly vanishes when n_t increases beyond $1/\varepsilon + 1$. We therefore choose n_t to be the integer part of $1/\varepsilon + 1$. Concerning the choice of the time step Δt between two images, we note that the temporal decay rate due to photobleaching is $\varepsilon/\Delta t$, while the relaxation (to equilibrium) rate due to diffusion is the inverse of the diffusion time $t_D = \ell^2/(16D)$ —defined as the time at which the standard deviation of the position of a Brownian particle reaches half the side length of the FRAPed region. If the time step Δt is too low, then fluorescence disappears before diffusion can be observed, whereas if the time step Δt is too high, most of the images are taken after diffusion has homogenized concentrations and these images are not informative. As a consequence, we expect the optimal delay between images to correspond to ε / $\Delta t \sim 1/t_D$. To further test this conclusion, we plotted in Fig. 3 the normalized empirical error $\Delta D_{\rm emp}/D_{\rm emp}$ as function of dimensionless delay $\Delta t/(t_D \varepsilon)$. As expected, the plot shows that the error $\Delta D_{\rm emp}$ has a minimum. This minimum occurs when $\Delta t \sim 10 t_D \varepsilon$, a value that we used in the remainder of this study.

The decay rate ε can also be reduced by decreasing the light dose delivered to the sample. In wide-field microscopy, this is typically achieved by modifying light intensity or the exposure time. In confocal microscopy, it can be controlled by adjusting the laser power or scanning speed. However, this decreased lighting reduces fluorescence, which deteriorates the signal/noise ratio at the detector. Altogether, it is unclear how changing the lighting conditions may affect the precision of HiFRAP.

Benchmarking HiFRAP

To test the efficiency of HiFRAP, we compared it with classical methods to obtain diffusion coefficient. Beforehand, we stress the versatility of HiFRAP because it makes no assumption on FRAP patterns or on boundary conditions, which is not the case of classical approaches. This is illustrated in Fig. S3, where the region FRAPped is axisymmetric with a Gaussian profile, X shaped or E shaped. For the comparison with other methods, which assume the bleaching pattern to be known, we considered a square FRAPped domain. Benchmarking was performed with respect to two classical approaches, as described in (6,20). The two approaches are based on determining the bleaching profile by fitting the postbleach image, and then estimating the diffusion coefficient by analyzing the recovery curve, i.e., the temporal variations of the signal average over the FRAPped region. For the first step, we followed (6) and modeled the square FRAPped profile as a 2D sharp function $f(x,y) = H(\ell/2 - x + x_0)H(x - x_0 + \ell/2)H(\ell/2)$ $(2-y+y_0)H(y-y_0+\ell/2)$ (with H the Heaviside function H(u) = 0 if u < 0 and H(u) = 1 if u > 0), smoothed to account for the point-spread function of the microscope. Accordingly the postbleach profile is parametrized by its size ℓ , the position of its center (x_0, y_0) , and the smoothing length. In a second step the two approaches differ. In the relaxation time-based method, the half-recovery time $\tau_{1/2}$ is estimated as the time at which the intensity has recovered half of its initial value in the FRAPped region (20). The diffusion coefficient is then computed using the theoretical relation $D_{\rm est}=0.923\,\frac{\ell^2}{16\tau_{1/2}}$ valid for a square FRAPped region. In the temporal fit-based method, the diffusion coefficient is obtained by fitting the recovery curve to the theoretical curve for a FRAPped region with side length and smoothing length, as obtained in the first step. The final formula is found in (6).

As the three methods retrieve the true diffusion coefficient on average, we compared their respective precisions. The empirical errors on diffusion coefficient are shown in Fig. 4 for different amplitudes of noise. The errors are computed for 200 artificial data sets for each noise strength. As could be expected, the empirical error increases with the noise strength. HiFRAP performs better than the two other approaches, especially at lower noise values, although HiFRAP does not make any assumption on the FRAPped bleaching profile. We ascribe the performance of HiFRAP to the fitting of spatiotemporal data instead of temporal data in other approaches. This comes with a higher computational cost for our approach. HiFRAP requires a few seconds to be run, depending on the number of Fourier modes n_q and temporal points n_t (see Fig. S2), whereas classical methods are almost instantaneous because models are fit to only n_t data points.

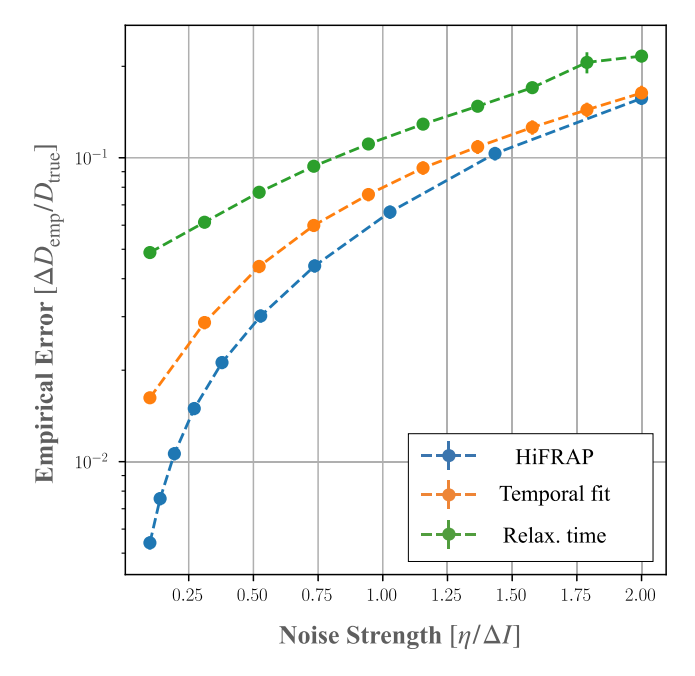


FIGURE 4 Benchmarking of HiFRAP. Empirical error $\Delta D_{\rm emp}$ as function of the noise strength η , the noise amplitude, normalized in terms of signal drop upon bleaching ΔI . The lines and relaxation time-based (green), temporal-fit-based (orange), and HiFRAP (blue) methods. Empirical error was computed as $\Delta D_{\rm emp} = \sqrt{\frac{n_{\rm ds}}{n_{\rm ds}-1}} \langle (D_{\rm est} - D_{\rm true})^2 \rangle$ from estimated values $D_{\rm est}$ and true value $D_{\rm true}$ of the diffusion coefficient from $n_{
m ds}=$ 200 number of data sets. . Error bars represent the estimated standard error of the empirical error.

Applying HiFRAP to reaction-diffusion

Our method can be generalized to infer kinetic parameters for more complex dynamics. Besides diffusion, molecules may be synthesized, degraded, or undergo other chemical reactions. In addition, membrane-localized proteins or lipids may be exocytosed or endocytosed. As long as the changes in concentration are not too large, the dynamics of one chemical species can be modeled by a linear diffusion-reaction equation,

$$\frac{\partial c}{\partial t} = D_{\text{true}} \nabla^2 c + \alpha_{\text{true}} - \beta_{\text{true}} c, \tag{2}$$

where D_{true} is still the diffusion coefficient, while α_{true} and β_{true} represent source rate and exchange rate, respectively, both assumed to be constant. The interpretation of these reaction terms depends on context. For instance, α_{true} may correspond to a synthesis rate and β_{true} to a degradation rate. In the case of a membrane-localized molecule, α_{true} and β_{true} may correspond to the rates of exocytosis and endocytosis, respectively, of this molecule. To extend HiFRAP to reaction-diffusion, we followed the same approach as in a method to infer parameters from FRAP experiments with the difference that the cost to minimize now depends on multiple parameters, D, α , β , and/ or ε . The minimization with respect to D, β , and ε is performed numerically using the reflective trust region algorithm, while α and I_{BG} are computed analytically (see inference in the case of reaction-diffusion with photobleaching for details). The imaging step can be optimized as in optimizing experimental and analysis parameters for a weak laser beam. Eq. 2 involves two characteristic times, the diffusion time t_D = $\ell^2/(16D_{\rm true})$, and the exchange time $t_{\beta} = \log(2)/\beta$. The typical recovery time t_r for the combined dynamics is expected to be of the order of $1/t_r = 1/t_D + 1/t_\beta$. Accordingly, the optimal time step can be taken as $\Delta t \sim \varepsilon t_r/10$.

We generated artificial reaction-diffusion data with the same initial square FRAP profile as before, as described in artificial data. Fig. 5 shows the inference of the parameters of Eq. 2 from these data using HiFRAP. We first assumed that the stationary solution c_s is perfectly known a priori, from the prebleaching images, for instance. When c_s is known, the cost function depends only on D and β (see inference in the case of reaction-diffusion with photobleaching). In Fig. 5A, we show an example of the contours of the cost function. The estimate on α may be obtained from the relation $\alpha_{\rm est} = c_{\rm s}\beta_{\rm est}$. To explore the behavior of our method, we would a priori need to vary D_{true} , α_{true} , and β_{true} . However, changing the ratio $\alpha_{\rm true}/\beta_{\rm true}$ only changes the stationary concentration and so does not affect the uncertainty of the different estimates. Changing the recovery time t_r does not significantly affect the precision of the method, since we adapt the time resolution of the experiment accordingly. We therefore varied the ratio t_{β}/t_D in Fig. 5, B and C, keeping $\alpha_{\text{true}}/\beta_{\text{true}}$ and t_r constant. As could be expected (39), the uncertainty on the diffusion coefficient becomes high when the fluorophore dynamics is dominated by reaction and, reciprocally, the uncertainty on the relaxation coefficient becomes high when the dynamics is dominated by diffusion. We note that, like in the pure diffusion case, the curvature of the cost function yields a good estimate of the error on parameters (see Fig. S1). Finally, we assessed the quality of the fit by comparing it with fits to diffusion only (assuming $\alpha_{\text{true}} = \beta_{\text{true}} = 0$) and reaction-only models (assuming $D_{\text{true}} = 0$) using the adjusted coefficient of determination R_{adj}^2 . Fig. 5 D shows that $R_{\rm adi}^2$ is always much larger for the reaction-diffusion model, meaning that it better explains the data, except for low or high ratios of reaction to diffusion times, for which the reaction-diffusion model is almost equivalent to one of the two simplest models.

When the values of rate of photobleaching during imaging, stationary concentration and background are unknown, they can be estimated together with the kinetic parameters using optimization in 5D space. Fig. 6 shows the results of HiFRAP in this case. Our estimates remain fairly good. The errors on diffusion and reaction coefficients behave like in the preceding case, although they are bigger here owing to the higher dimensionality (5 instead of 2). The errors on the source rate, bleaching rate, and background increase when the fluorophore dynamics is dominated by diffusion, similar to the exchange rate because all three parameters effectively relate to reactions.

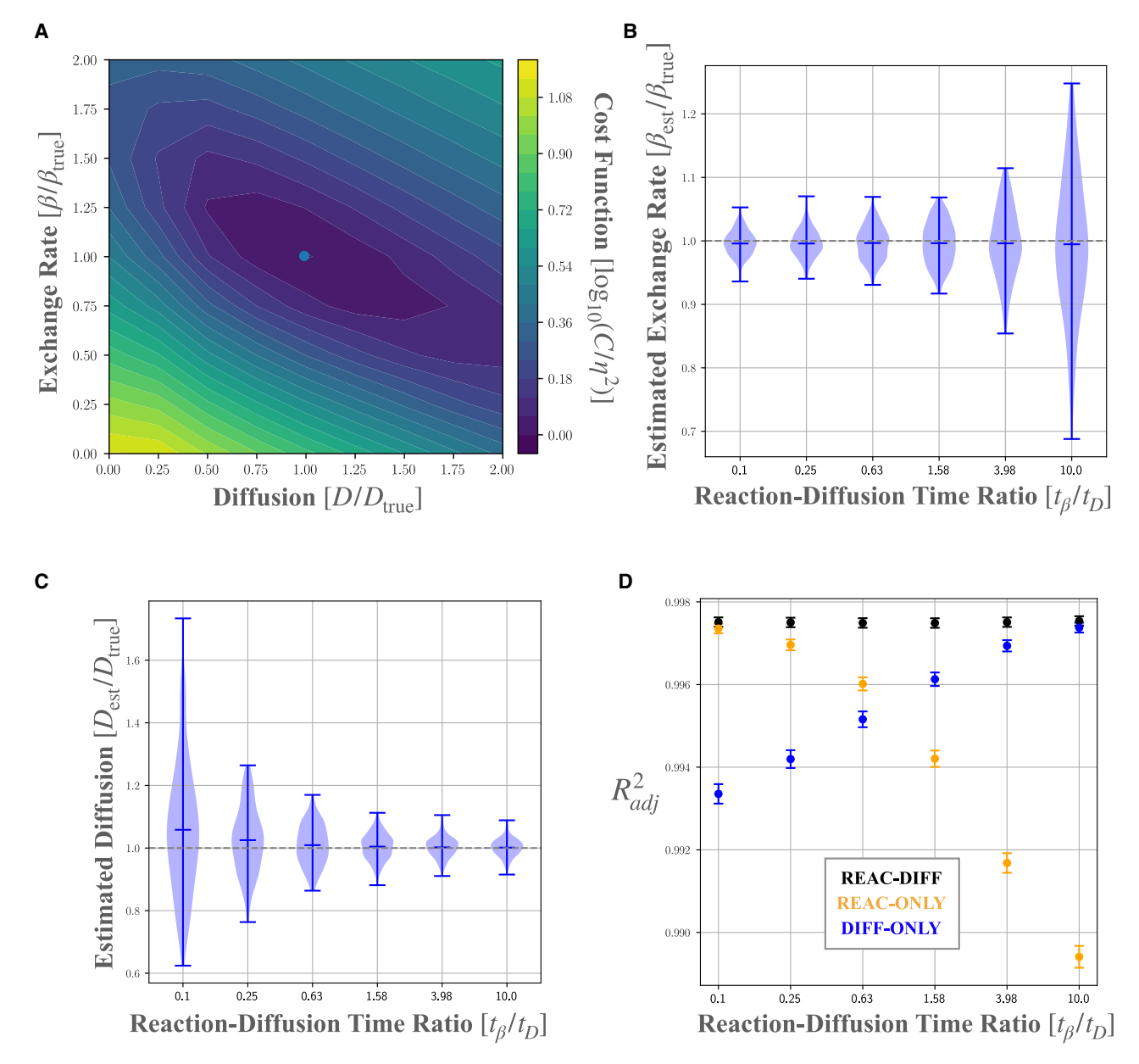


FIGURE 5 HiFRAP applied to the estimation of diffusion and reaction rates knowing the pre-FRAP concentration field and the rate of photobleaching during imaging. (A) Contour plot of the normalized cost function ($\log_{10}[C/\eta^2]$, with η the amplitude of the noise) as a function of the normalized fitting parameters D/D_{true} and $\beta/\beta_{\text{true}}$, while the source term α is constrained to be $\alpha = \beta c_s$, with c_s the stationary concentration known from prebleaching images. The colorscale is shown on the right, with blue and yellow corresponding to low and high cost, respectively. The light blue point indicates the minimum of the cost function; its coordinates yield the estimates D_{est} and β_{est} . (B and C) Estimated dynamical parameters D_{est} and β_{est} as function of the reaction-diffusion time ratio $t_{\beta}/t_{D}=16\log(2)/\ell^{2}D_{\text{true}}/\beta_{\text{true}}$ keeping the signal relaxation time $t_{r}=\left(1/t_{\beta}+1/t_{D}\right)^{-1}=\varepsilon\Delta t/7$ constant. Violin plots show the distribution of the estimates and horizontal ticks indicate the maximum, the average, and the minimum of the distribution. The dashed gray line represents the reference value at which the estimated parameter is equal to the true parameter of the system. Here, the stationary concentration, c_s, is assumed to be known from the average pre-FRAP concentration field, so that $\alpha_{\rm est} = c_s \beta_{\rm est}$. The rate of photobleaching during imaging, ε , is supposed to be known from a control area. The number of data sets analyzed is 200. (D) Adjusted coefficient of determination, R_{adj}, for three different fits, diffusion only, reaction only, and reaction-diffusion, as a function of reaction-diffusion time ratio. The error bar represents the mean and the standard deviation of the distribution.

Applying HiFRAP to experimental data

We implemented HiFRAP as an ImageJ macro that wraps Python scripts (available on https://github.com/ lorenzetti1996/HiFRAP_project). Here, we illustrate the macro with experiments in fission yeast. We considered a putative mechanosensitive transmembrane protein, Mtl2p, which is homogeneously distributed around the cell surface (46). We prepared and imaged cells as detailed in experiments. Given that Mtl2p has very low cytoplasmic

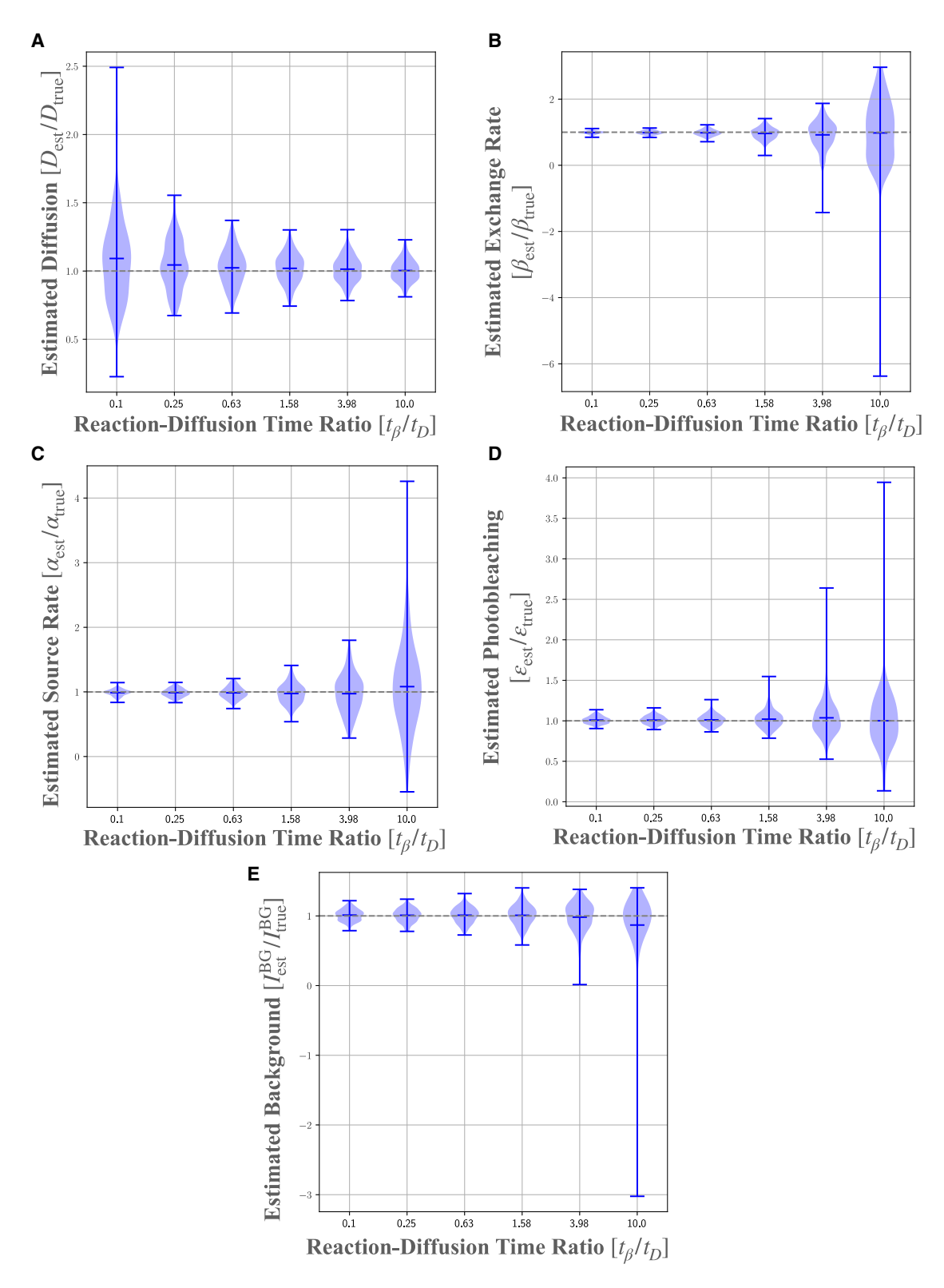


FIGURE 6 HiFRAP applied to diffusion-reaction when pre-FRAP concentration field and rate of photobleaching during imaging are unknown. Distributions of the estimated parameters (normalized by their true values) as a function of the reaction-diffusion time ratio t_{β}/t_{D} for 200 artificial data sets: (A) diffusion coefficient $D_{\rm est}$, (B) exchange rate β_{est} , (C) source rate $\alpha_{\rm est}$, and (D) rate of photobleaching during imaging ε and E background signal intensity $I_{\rm BG}$. Violin plots show the distributions. The horizontal ticks stand for the maximum, the average, and the minimum of the distributions. The dashed gray line represents the reference value at which the estimated parameters is equal to the true value of the system.

concentration, we hypothesized that, over the timescale of experiments, Mtl2p diffuses along the surface of the cell, and we aimed at testing this hypothesis and at estimating the diffusion coefficient.

Building upon preceding sections, we implemented the HiFRAP ImageJ macro for three models (diffusion only, reaction-diffusion, or reaction only) and for various experimental options. These options include the potential use of additional information to reduce errors on the estimation of parameters, see improving parameters estimation using extra-information for details. In particular, HiFRAP enables to select two regions outside the ROI (contains the FRAPped domain): a region free from fluorescent reporters (background ROI)—used to estimate the background value I_{BG} by averaging, and an unFRAPped region (control ROI)—used to estimate the rate of photobleaching during imaging ε . Fig. 7 A shows three example ROIs for a 2D FRAP geometry. The ROIs were chosen as large as possible to maximize the amount of information analyzed, within the constraint of being not too close to cell edges (as viewed from the top) or to image edges, to avoid the effects of, respectively, cell curvature and optical distortion on signal intensity. Potential additional information also includes prebleaching images, which yield stationary molecule concentration c_s by averaging. In cases where FRAP is performed in a 1D geometry, the user selects polylines instead of rectangular regions to define the control and FRAP areas. These polylines are then straightened using ImageJ's built-in algorithm to create a linear representation: a user-defined width is used to extract and average pixel intensities perpendicular to the path, generating a 1D intensity profile for each image.

In FRAP experiments on Mtl2p-GFP, typical estimates are $I_{\rm BG} \approx 100~[A.U.]$ for the background level (from the background ROI), $c_s \approx 30~[A.U.]$ for the stationary concentration (using one prebleaching image), and $\varepsilon \sim 10^{-2}$ for the photobleaching (using the control ROI). In Fig. 7, B and C we show the same plots as in Fig. 1 for the estimation of the diffusion coefficient from one FRAP experiment. The cost function presents a single minimum (C) and the corresponding best fit to compressed experimental data is shown in the third row of (B).

We optimized experimental parameters following optimizing experimental and analysis parameters. The size of the ROI being limited by cell width, we chose to use square ROIs of side length $\sim 1.5~\mu m$ and FRAPped square regions of side length $\ell \sim 0.5~\mu m$. In practice, we found that the initial bleaching profile was imperfect; the reduction in signal intensity was inhomogeneous and did not occur over a perfect square (see t=0 in Fig. 7 B). This may be caused by different factors such as the small size of the FRAPped region, laser imprecision, or fluctuations in fluorophore concentration. To adjust the imaging time step Δt , we first estimated the order of magnitude of the diffusion co-

efficient and of photobleaching rate per image by applying HiFRAP to a preliminary experiment. We found $\varepsilon \sim 10^{-2}$ and $D_{\rm est} \sim 10^4~\mu {\rm m}^2 {\rm s}^{-1}$. Then, to optimize our analysis, we chose $\Delta t = (5/8)~\varepsilon \ell^2/D \sim 10~{\rm s}$, and $n_t = 1/\varepsilon \simeq 100$. Finally, to limit the computational cost, we used $n_a = 9$ modes for the compression.

Following parameter adjustment, each of the 18 analyzed cells was FRAPped once. We fitted experimental data to each of the three models: diffusion only, reaction-diffusion, and reaction only. Estimated parameters are given in Table 1. To assess whether the dynamics of Mtl2p-GFP is dominated by diffusion or by reaction, we computed the adjusted coefficient of determination R_{adj}^2 , as shown in Fig. 7 D. In all the 18 experiments, the diffusion model has a higher $R_{\rm adi}^2$ compared with the reaction model, indicating that diffusion contributes more to Mtl2p dynamics at the experimental timescale; the diffusion-reaction model has slightly higher R_{adi}^2 than the diffusion only model, suggesting that the two are almost equally good at explaining the data. Consistently, the Kolmogorov-Smirnov test rejects the reaction model (the p value is greater than 0.05 for 60% of the cases, well below the threshold of 95%) and tends to reject the reaction-diffusion model. In addition, when considering a reaction-diffusion model, we find an average loss rate that is not positive, which is not physically acceptable because it means, for instance, that the rate of detachment of Mtl2p from the membrane is negative. For this reason, we conclude that pure diffusion better explains experimental data.

Considering a diffusion model, we found an average value of the diffusion coefficient, $\langle D^{est} \rangle = 1.93 \ 10^{-4} \mu \text{m}^2 \text{s}^{-1}$, lower than diffusion coefficients of proteins in animal cell membranes (2), but in agreement with the order of magnitude $10^{-4} - 10^{-2} \mu \text{m}^2 \text{s}^{-1}$ for membrane-localized proteins in budding yeast or in fission yeast (12,49–52). Such low value of surface diffusion coefficient is likely due to the presence of a cell wall (53). We also note that the empirical error—i.e., the standard deviation of the diffusion coefficient over all experiments— $\Delta D_{\text{emp}} = 1.40 \ 10^{-4} \mu \text{m}^2 \text{s}^{-1}$, is much greater than the estimated error in single experiments $\langle \Delta D_{\text{est}} \rangle = 0.07 \ 10^{-4} \ \mu \text{m}^2 \text{s}^{-1}$. This reflects biological cell-to-cell variability in diffusion, which has already been observed in cultured animal cells based on single-particle tracking (54).

CONCLUSION

We have developed HiFRAP, a method to infer reaction (or exchange)-diffusion kinetic parameters from FRAP with imperfect conditions, and we have implemented it as a Fiji plugin. HiFRAP leverages the full spatiotemporal information contained in the time-lapse sequence to derive kinetic parameters, errors on these parameters, and a test of model validity so as to select which model better explains experimental observations.

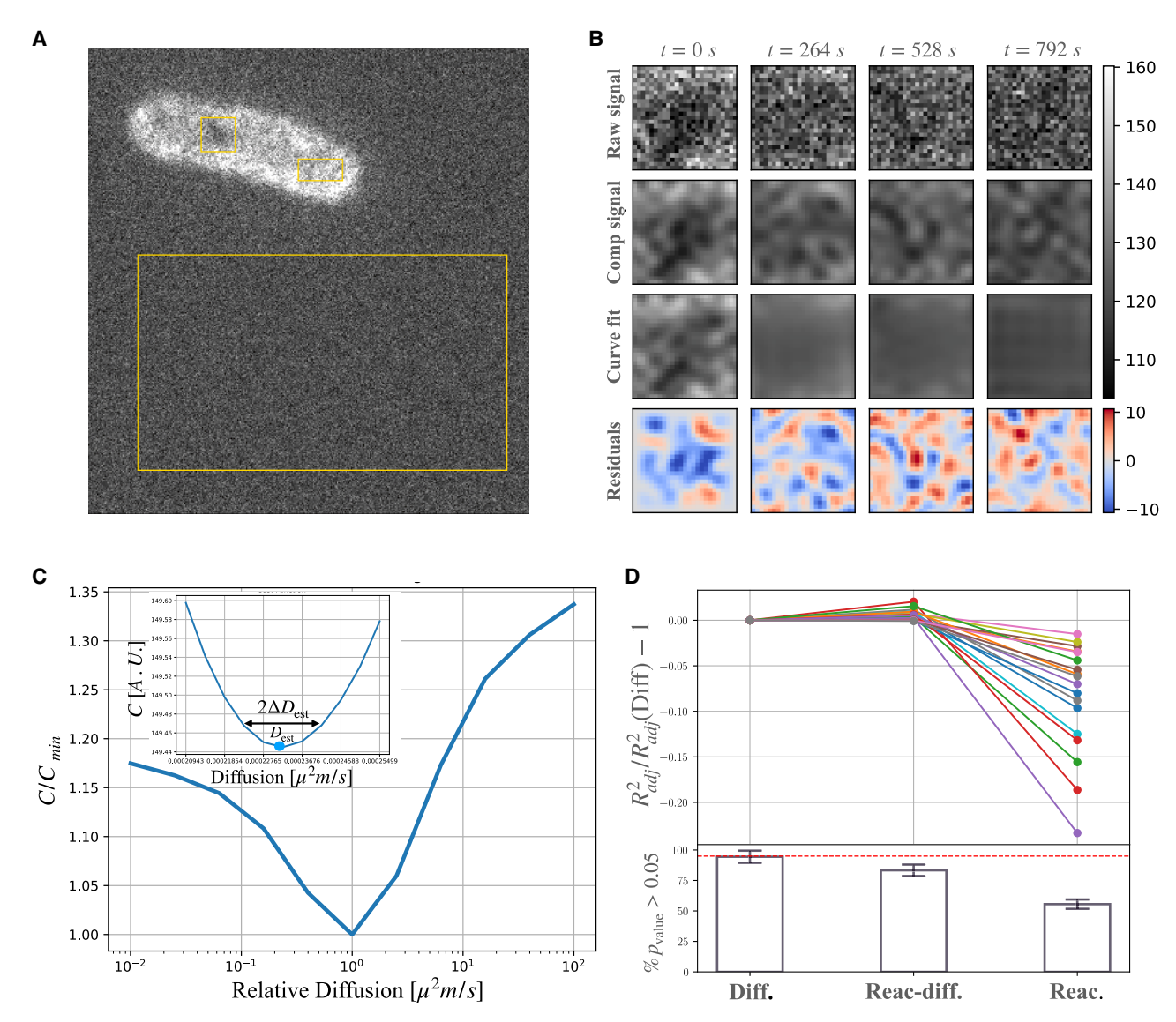


FIGURE 7 Inferring the diffusion coefficient from experimental data. (A) Fluorescence microscopy image of a fission yeast cell expressing Mlt2-GFP. The cell was bleached inside a region to the left of the cell center. Three regions were selected with Fiji. The square is the region of interest that contains the FRAPped region and has side length = $1.45 \, \mu \text{m}$. The top rectangle is the control ROI, used to estimate rate of photobleaching during imaging. The bottom rectangle is the background ROI, used to estimate background signal intensity. (B) From experimental signal to fit; two-dimensional data shown at four time points—time in seconds is indicated above the first row, t = 0 follows initial bleaching. From top to bottom: experimental data inside the ROI; compressed experimental data; fit to compressed experimental data; residuals of the fit. The grayscale and colorscale are shown on the right. (C) Corresponding cost function C (normalized by its minimum) as a function of fitting parameter D (normalized by the estimated diffusion coefficient D_{est}) for the diffusion coefficient; the inset is a zoom-in around the minimum with the cost function in the arbitrary unit of the signal and the diffusion values in μ m²/s. (D) Assessing the goodness of the diffusion model by comparing it with reaction-diffusion and to reaction-only models. Top: adjusted coefficient of determination R_{adj}^2 normalized using its value for the diffusion model; each line corresponds to one of the 18 experiments (one color per experiment). Kolmogorov test (bottom): each bar indicates the fraction of cases in which the Kolmogorov test was above the 0.05 value; the red dashed line indicates the level below which the model should be rejected; error bars correspond the error in sampling a binomial distribution.

HiFRAP combines all useful features that have been developed separately in previous work. HiFRAP makes it possible to infer several parameters from a single FRAP experiment (6,13,19,36–38,40–45), as long as system dynamics is sufficiently sensitive to these parameters (39). We make no assumption on the bleaching profile

(21–24,27,42,44) nor on boundary conditions; HiFRAP is thus well-suited experimental conditions in which it is difficult to bleach uniformly the target region or to be far from boundaries. Moreover, due to its versatility, our method is applicable to all the FRAP variants discussed (spot, strip, and iFRAP), even though the source

TABLE 1 Estimated parameters (mean ± standard deviation over 18 experiments) and associated errors for each model

Parameter	$\langle D_{ m est} angle$	$\langle \sigma_D^{ m est} angle$	$\langle eta_{ m est} angle$	$\langle \sigma_{eta}^{ m est} angle$	$\langle lpha_{ m est} angle$	$\langle \sigma_{lpha}^{ m est} angle$
Unit	$10^{-4} \mu \text{m}^2/\text{s}$	$10^{-4} \mu \text{m}^2/\text{s}$	$10^{-4} s^{-1}$	$10^{-4} s^{-1}$	AUs^{-1}	AUs^{-1}
Diffusion	1.93 ± 1.40	0.07 ± 0.06	_	_	_	_
Reaction-diffusion	3.3 ± 3.2	0.2 ± 0.2	-10 ± 16	2 ± 1	-0.18 ± 0.29	0.03 ± 0.02
Reaction	_	_	9.4 ± 4.5	0.5 ± 0.2	0.166 ± 0.100	0.008 ± 0.003

From left to right: diffusion coefficient $D_{\rm est}$, error on diffusion $\sigma_D^{\rm est}$, exchange rate β , error on loss $\sigma_{\beta}^{\rm est}$, source rate $\alpha_{\rm est}$ (AU stands for arbitrary unit), and error on source $\sigma_{\alpha}^{\rm est}$. From top to bottom: reaction only, reaction-diffusion, and reaction-only models.

term for the reaction is zero in the case of the photoconversion configuration. Furthermore, HiFRAP accounts for intrinsic photobleaching associated with repeated imaging, either based on a control region or on inference of photobleaching rate (23,26,42). Finally, HiFRAP integrates three features that do not seem to have been implemented before: errors on parameter estimation for a single experiment; diffraction in the microscopy setup although the precise characteristics of the point-spread function are not required as long as its width is larger than pixel size; test of model goodness. We ran HiFRAP against classical benchmarks and found that HiFRAP provides lower or equal errors despite being more general. Although relying on advanced inference techniques, HiFRAP remains accessible: a user-friendly macro allows experimentalists to perform the analysis with only a minimal understanding of the underlying theory (such as the number of compression modes), which are the only user-defined inputs required.

However, HiFRAP has a few limitations. First of all, HiFRAP is relatively slow (execution time of a few seconds with standard parameters and standard computer). Most available methods do not explicitly deal with noise. We were led to make the simplifying assumption that noise is homogeneous and stationary, which is not necessarily true (42,55). For example, the amplitude of the shot noise associated with photon counting is proportional to the square root of the signal. Such spatiotemporal variation of noise would likely affect error estimation but not parameter estimation.

In principle, HiFRAP can be adapted to FRAP variants, involving, for instance, continuous photobleaching of a region or photoconversion of a fluorophore (5), and to the FRAP analysis of other types of dynamics, such as advection by active transport (13,45), subdiffusion (29,30), multiple-species (13,39,42), and nonflat geometries (9,28). HiFRAP assumes linearity of underlying PDEs, but this is not a strong limitation as the dynamics becomes quickly linear upon return of the system to its equilibrium state. Currently, HiFRAP cannot handle 3D geometries, multispecies models, or systems involving advection phenomena and it assumes an image acquisition time much smaller than molecule dynamics. However, future developments may address these limitations, enabling broader applicability of the method.

Our method is actually not restricted to FRAP and could be used for inference of parameters for any linear PDE based on the effects of a perturbation on the system. We can therefore expect applicability of our method to capillary isoelectric focusing (56) or to optogenetics (57). Overall, our approach can be considered as a good alternative to machine learning approaches since it does not require training (58).

MATERIALS AND METHODS

Data sampling and compression

Here and elsewhere, we present our methodology for a 2D system, which also applies to a 1D system unless specified. The notations used troughout this section are summurized in Table 2. We consider a spatiotemporal signal collected at discrete positions $(X^{(1)}, X^{(2)})$ such that $X^{(1)} = X^{(2)} = [0, \Delta x, ..., (n_x - 1)\Delta x]$ and times $T = [0, \Delta t, ..., (n_t - 1)\Delta t]$, where Δx is the spatial mesh size and Δt is the time step, $n_x \times n_x$ is the number of pixels and n_t the number of time frames. We vectorize the measurements by arranging them into a unique vector $\{I_k^{DATA}\}_{k=1}^{N_{tot}}$ composed of $N_{tot} = n_x^2 n_t$ elements, where the index $k = a + bn_x + cn_x^2$ is associated to the space-time triplet $(x_k^{(1)}, x_k^{(2)}, t_k) = (X_a^{(1)}, X_b^{(2)}, T_c), X_a^{(p)}$ and T_a being the a-th components of the vectors $X^{(p)}$ and T_a , respectively. We assume that the empirical data correspond to a theoretical spatiotemporal signal c(x, y, t) that can be sampled into a theoretical data vector through the sampling operator $S: c(x,t) \longleftrightarrow \{I_k^{TH}\}_{k=1}^{N_{tot}}$, defined as $I_{a+bn_x+cn_k}^{TH} = c(X_a^{(1)}, X_b^{(2)}, T_c)$.

To save data storage space and computational time, we compress these vectors into smaller vectors made of N elements $(N < N_{tot})$, defining the compression operator $C: \{I_k\}_{k=1}^{N_{tot}} \longleftrightarrow \{Y_i\}_{i=1}^{N}$. In practice, we chose to compress in the space domain because $n_x \times n_x$ is in general much greater than n_t : We keep n_q spatial Fourier coefficient per axis, so that $N = n_q^2 n_t$. Accordingly, we define the compression operator as

$$C: Y_i = \sum_{k=1}^{N} F_{i,k} \delta_{t_i/\Delta t, t_k/\Delta t} I_k$$
 (3)

where $\delta_{i,k}$ is Kronecker's delta and the Fourier matrix has elements $F_{i,k} = \tilde{F}(q_i^{(1)}, x_k^{(1)}) \tilde{F}(q_i^{(2)}, x_k^{(2)})$ with

$$\tilde{F}\left(q_{i}^{(p)}, x_{k}^{(p)}\right) = \frac{1}{\sqrt{n_{x}}} \begin{cases}
\frac{1}{\sqrt{2}} \cos\left(q_{i}^{(p)} x_{k}^{(p)}\right) & \text{if } q_{i}^{(p)} < 0 \\
1 & \text{if } q_{i}^{(p)} = 0 \\
\frac{1}{\sqrt{2}} \sin\left(q_{i}^{(p)} x_{k}^{(p)}\right) & \text{if } q_{i}^{(p)} > 0
\end{cases} \tag{4}$$

TABLE 2 Notations for sampling and preprocessing

n_{χ}	Number of pixels per axis		
$\overline{n_t}$	number of time frames (of 2D images)		
Δx	pixel size		
Δt	time interval between two frames		
c(x,t)	concentration field (function of space and time)		
$c(x,t)$ I_k^{DATA}	raw data vector		
I_k^{TH}	noiseless theoretical data vector		
Y_i^{DATA} Y_i^{TH} S	preprocessed (compressed) data vector		
Y_i^{TH}	noiseless theoretical preprocessed data vector		
Š	sampling operator, maps concentration field onto		
	raw data vector		
С	compression operator, maps raw data vector onto		
	preprocessed vector		
F	spatial Fourier transform matrix		
n_q	number of spatial modes kept per axis after		
-	compression		

where the index i is associated to the Fourier-temporal vectorization with the Fourier vector of each axis spanning the value $Q^{(1)}=Q^{(2)}=\frac{\pi\Delta x}{n_x-1}\left[-\frac{n_q-1}{2},\ldots,0,\ldots,\frac{n_q-1}{2}\right]$

The results in Fig. S2 show that, as long as $n_q \geq 3$, compression affects neither the accuracy—how close the mean of the distribution of the estimated parameter is to the true value—nor the precision of the estimation—the variance of the estimated parameter distribution. Typically, $n_q \geq 5$ is sufficient to reach 80% of the precision that would be obtained without compression.

Inferring dynamical parameters

Problem formulation

In this section and the following ones, we detail the method used to estimate the dynamical parameters. To help the reader, we gathered all mathematical notations introduced through the inference procedure in Table 3. Our aim is to estimate the vector $\vec{\theta} = \{\theta_1, ..., \theta_n\}$ of the parameters of a linear PDE from an empirical signal $\{Y_i^{DATA}\}_{i=1}^N$. We consider system dynamics after a linear perturbation w(x). The theoretical, noiseless solution to the PDE takes the form

$$Y_i^{TH} \left\{ \vec{\theta}, w \right\} = \int_{\mathbb{R}^2} \mathcal{G}_i \left(\vec{\theta}, y \right) w(y) dy + h_i \left(\vec{\theta} \right), \tag{5}$$

where the linear operator \mathcal{G} (related to Green's function) and the shift vector h are specific to the PDE. As we will see later, it is also possible to include in \mathcal{G}_i the effect of any linear operation on the signal, such as spatial filtering by the optical setup.

We consider experimental/technical noise, defined as $e_i = Y_i^{DATA} - Y_i^{TH}(\vec{\theta}_{\text{true}}, w_{\text{true}})$, where θ_{true} and w_{true} are the true parameters and initial condition. We assume that the e_i are uncorrelated, i.e., $\langle e_i e_j \rangle = \delta_{i,j} \eta^2$, where $\delta_{i,i}$ is the Kronecker delta and η the unknown noise amplitude.

Fitting the initial condition at fixed model parameters

Under these hypotheses, we can estimate the vector $\vec{\theta}$ resorting to the least-squares method, which consists in minimizing a cost that quantifies the differences between observed data set and theoretical solution $Y_i^{DATA} - Y_i^{TH}(\theta,w)$. Since the initial profile w is not known, at any given θ , we first estimate it by minimizing the cost $C_{\text{tot}} = \sum_{i=1}^{N} \left(Y_i^{DATA} - Y_i^{TH}(\theta,w)\right)^2$ with respect to w. By exploiting the fact that the theoretical solution (5) is linear in w, this operation can be performed analytically, yielding

TABLE 3 Notations for inference

$\overrightarrow{\theta}$	Vector of kinetic parameters to be inferred		
$\overrightarrow{\theta}_{\text{true}}$	vector of true values of kinetic parameters		
$\overrightarrow{\theta}_{\text{est}}$	vector of estimated kinetic parameters		
w	spatial perturbation		
Gw + h	the linear operator \mathcal{G} and the shift vector h		
e_i	noisy part of the preprocessed vector		
η	amplitude of the noise		
K	kernel operator		
K^+	pseudoinverse of the kernel operator		
λ	small positive number to ensure matrix inversion or		
	threshold on eigenvalues		
$U_R U_R^T$	reduced kernel by SVD truncation along each axis		
$N_{\it eff}$	trace of $[\lambda K^+]^2$ representing the effective degrees of		
	freeedom		
Φ	null matrix associated with kernel operator		
r	residual between data and theory vector after fitting		
	the initial condition at $\overrightarrow{\theta}$ fixed		
\tilde{r}	projected residual in the null space generated by $\boldsymbol{\Phi}$		

$$\min_{w} \sum_{i=1}^{N} \left[Y_{i}^{DATA} - h_{i} \left(\vec{\theta} \right) - \int_{\mathbb{R}^{2}} \mathcal{G}_{i} \left(\vec{\theta}, y \right) w(y) dy \right]^{2}$$

$$=\sum_{i=1}^{N} \left[r_i (\vec{\theta}) \right]^2 \tag{6}$$

where the residual vector r, which represents the difference between the data vector and the constrained fit at fixed θ , is given by

$$r(\vec{\theta}) = \lambda K^{+}(\vec{\theta}) (Y^{DATA} - h(\vec{\theta})).$$
 (7)

 K^+ is the pseudoinverse of the kernel matrix K (59)

$$K_{i,j} = \int_{\mathbb{R}^2} dy \mathcal{G}_i(\vec{\theta}, y) \mathcal{G}_j(\vec{\theta}, y).$$
 (8)

We use the pseudoinverse K^+ ,

$$K^+ = (K + \lambda Id)^{-1} \tag{9}$$

because the kernel matrix K is not definite positive. The small positive number λ ensures that the pseudoinverse is well defined. We take $\lambda = N\sigma_0\epsilon$, using the largest eigenvalue σ_0 of the kernel matrix K and machine precision ϵ (60), yielding typical values of $\lambda(\vec{\theta})$ in the range 10^{-11} to 10^{-12} .

Kernel reduction

To accelerate the computation of the pseudoinverse in Eq. 7, we take advantage of the fact that multidimensional problems can often be reformulated in terms of smaller matrices that describe the structure of the kernel along each spatial direction. As we will see in inference in the case of pure diffusion without photobleaching for diffusion and inference in the case of reaction-diffusion with photobleaching for reaction-diffusion, the kernel matrix can be factorized as

$$K_{i,j} = \kappa \left(q_i^{(1)}, t_i, q_j^{(1)}, t_j \right) \kappa \left(q_i^{(2)}, t_i, q_j^{(2)}, t_j \right)$$
(10)

The values of the function κ at $(q_i^{(\ell)}, t_i, q_j^{(\ell)}, t_j)$, with $\ell \in \{1, 2\}$, are collected in a matrix $\kappa^{(\ell)}$ of dimension $n_q n_t \times n_q n_t$, whose *u*-th row and v-th column are mapped by the relations $u = a + cn_q$, $v = a' + c'n_q$ for $\kappa^{(1)}$ and $u = b + cn_q$, $v = b' + c'n_q$ for $\kappa^{(2)}$, where a, b, c are associated to the triplet $(q_i^{(1)},q_i^{(2)},t_i)=(Q_a^{(1)},Q_b^{(2)},T_c)$ and $a',\ b',\ c'$ to $(q_i^{(1)}, q_i^{(2)}, t_j) = (Q_{a'}^{(1)}, Q_{b'}^{(2)}, T_{c'})$ as previously defined in data sampling and compression.

Using singular value decomposition (SVD)-based truncation (61), we approximate the matrices $\kappa^{(\ell)}$ by considering the n_K eigenvalues σ_k , $k \in$ $\{0,...,n_K-1\}$, larger than the same threshold $\lambda=n_qn_t\epsilon\sigma_0$ as for the pseudoinverse and the associated eigenvectors $U_k(q_i^{(\ell)}, t_i)$. This operation yields

$$K_{i,j} \approx \sum_{k,k'=0}^{n_K} U_k \left(q_i^{(1)}, t_i \right) U_{k'} \left(q_i^{(2)}, t_i \right) \sigma_k \sigma_k' U_k \left(q_j^{(1)}, t_j \right)$$

$$U_{k'} \left(q_j^{(2)}, t_j \right) = \sum_{k''=0}^{n_K^2} [U_R]_{i,k''} [U_R]_{j,k''}$$
(11)

where U_R is a matrix of size $n_q^2 n_t \times n_k^2$, with components $[U_R]_{i,k''}$ $U_k(q_i^{(1)},t_i)U_{k'}(q_i^{(2)},t_i)\sqrt{\sigma_k\sigma_k'}$ with $k''=k+n_kk'$. Under this approximation, exploiting the Woodbury matrix identity, the pseudoinverse takes

$$\lambda K^{+} \approx Id - \left[U_{R} \left(U_{R}^{T} U_{R} + \lambda Id \right)^{-1} U_{R}^{T} \right],$$
 (12)

which is much faster to compute compared with its full expression since the size of the matrix $U_R^T U_R + \lambda Id$ is smaller than the size of $K + \lambda Id$ by a factor of ~ 10 with the parameters used here. We note that, because of the definition of λ , the errors induced by the approximations above are of the order of machine precision and so are negligible. In practice, we use this approximation of the pseudoinverse K^+ for a 2D system, but not in dimension 1 because the computational gain is limited, in which case we directly compute the pseudoinverse of the kernel matrix as given by Eq. 9.

Fitting model parameters

The next step would be to minimize the sum of the squared residuals (Eq. 7) with respect to $\vec{\theta}$. However, the average contribution of the noise vector $\{e_i\}_{i=0}^N$ to the residuals $\{r_i\}_{i=0}^N$ scales with the effective degrees of freedom $N_{eff}(\vec{\theta}) = \lambda^2 \sum_{i=0}^{N} [K^+]_{i,i}^2$ associated with the fit of the initial condition (62) whose value varies according to $\vec{\theta}$. For this reason, to avoid biasing the inference toward values of $\vec{\theta}$ that require stronger constraints for the initial condition fit (indicated by a lower number of effective degrees of freedom), we normalize the sum of residuals squared in Eq. 7 by $N_{eff}(\vec{\theta})$. Combining this normalization with Eqs. 7 and 9, we obtain the estimation of the parameter vector by minimizing the cost $C(\vec{\theta})$ as

$$\vec{\theta}_{\text{est}} = \arg\min_{\vec{\theta}} C(\vec{\theta}) \text{ with } C(\vec{\theta})$$

$$= \frac{1}{N_{\text{eff}}} \sum_{i=0}^{N} \left(\sum_{j=0}^{N} K_{i,j}^{+} (Y_{j}^{DATA} - h_{j}) \right)^{2}, \qquad (13)$$

where N_{eff} , K^+ , h, and λ all depend on $\vec{\theta}$.

For a 2D system, the kernel reduction $K \approx U_R U_R^T$ is used to compute both the pseudoinverse, based on Eq. 12, and the effective degrees of freedom at the denominator of Eq. 13, based on $\lambda^2 \sum_{i,j}^N [K^+]_{i,j}^2 \approx N - n_k^2 +$ $\lambda^2 \sum_{k,k'}^{n_k^2} ([U_R^T U_R + \lambda Id]_{k,k'}^{-1})^2$. For a 1D system, the cost in Eq. 13 is directly computed with the primary definition of the kernel (Eq. 8).

Error on parameter estimation and goodness of the fit

Once the parameters $\vec{\theta}_{est}$ have been inferred by minimizing the cost function (Eq. 13), the error on their estimation can be calculated using a quadratic expansion of the cost function around its minimum, yielding an estimated error matrix

$$\left\langle \left(\vec{\theta}_{\text{est}} - \left\langle \vec{\theta}_{\text{est}} \right\rangle \right) \otimes \left(\vec{\theta}_{\text{est}} - \left\langle \vec{\theta}_{\text{est}} \right\rangle \right) \right\rangle \\
= \frac{2}{N_{\text{eff}} \left(\vec{\theta}_{\text{est}} \right)} \mathcal{H}^{-1} C \left(\vec{\theta}_{\text{est}} \right), \tag{14}$$

where \mathcal{H} is the Hessian of the cost function with respect to $\vec{\theta}$ evaluated at

We used two approaches to assess the goodness of the fit. The first is based on the adjusted coefficient of determination, which is the coefficient of determination (usually denoted by R^2) corrected using the number of degrees of freedom-this avoids a spurious increase of the coefficient of determination with the number of fitting parameters (63). In our case, the adjusted $R_{\rm adj}^2$ takes the form

$$R_{\text{adj}}^{2} = 1 - \frac{C\left(\vec{\theta}_{est}\right)}{\sum_{i=0}^{N} \left(Y_{i}^{DATA} - n_{x}\delta_{q_{i}^{(1)},0}\delta_{q_{i}^{(2)},0}\langle I^{DATA}\rangle\right)^{2}} \frac{N_{eff}\left(\vec{\theta}_{est}\right)(N-1)}{N_{eff}\left(\vec{\theta}_{est}\right) - n_{\theta}}$$

$$\tag{15}$$

where $C(\vec{\theta}_{est})$ is the minimum of the cost function (Eq. 13), $\langle I^{DATA} \rangle$ is the average of the raw data vector, and n_{θ} the length of the vector $\vec{\theta}$. Larger (and closer to 1) R^2 means a better fit (as this corresponds to smaller minimum of the cost function). This test can be used to compare different models, e.g., diffusion and reaction, for the same data set Y^{DATA} ; the model with larger R^2 should be favored. However, the adjusted R^2 cannot be used for an absolute evaluation of the goodness of the fit because the standard deviation of the data vector may vary from experiment to experiment, in particular with the shape and depth of the initial bleaching

For an absolute evaluation of the goodness of the fit, we used a Kolmogory-Smirnov statistical test as follows. The starting point is that multiplication by λK^+ in Eq. 7 approximately corresponds to projection on the orthogonal space of the matrix K (or of U_R in the case of kernel reduction). As consequence, the residuals can be approximated as $r_i \approx \sum_{p=0}^{n_p} \sum_{j=0}^{N} \Phi_{i,p} \Phi_{j,p} (Y_j^{DATA} - h_j)$, where the columns of the null matrix Φ (size $n_p \times N$) are the eigenvectors of K (or left eigenvectors of U_R) associated with eigenvalues above the threshold $\lambda = N\sigma_0\epsilon$. If we define the projected residual as $\tilde{r}_p = \sum_{j=0}^N \Phi_{j,p}(Y_j^{DATA} - h_j), \tilde{r}_p$ computed at $\vec{ heta}_{ ext{true}}$ depends only on the noise contribution $e_i = Y_i^{ ext{DATA}} - Y_i^{ ext{TH}}(\vec{ heta}_{ ext{true}})$ because $\sum_{j=0}^{N} \Phi_{j,p}(\vec{\theta}_{\text{true}}))(Y_j^{DATA} - h_j(\vec{\theta}_{\text{true}})) \approx 0$. Therefore, since $\tilde{r}_p(\vec{\theta}_{\text{true}}) \approx \sum_j \Phi_{j,p}(\vec{\theta}_{\text{true}}) e_j$ is a large linear combination of uncorrelated noise, the projected residuals computed at the true kinetic parameter values should be normally distributed. Accordingly, we apply the Kolmogorov-Smirnov normality test (48) to the vector \tilde{r} . We test the hypothesis that the model is compatible with the data by testing the null hypothesis that the reduced residuals are normally distributed. As can be seen in Fig. S5, we obtain a p_{value} smaller than 0.05 only for 5% of the simulations, as expected when the artificial data correspond to the model tested. However, this method is much slower compared with the adjusted R^2 , as the computation of eigenvectors scales with $\mathcal{O}(N^3)$, while the computation of the standard deviation scales with $\mathcal{O}(N)$.

Modeling signal acquisition

Here, we aim at accounting for two experimental features: photobleaching during imaging associated with imaging and diffraction in the optical setup. When the sample is imaged, photobleaching occurs at a rate ε per image. Diffraction implies that the detectors collect the true signal convolved by the point-spread function, assumed to be a Gaussian of width μ as a point-spread function. The sampling operator can then be expressed as

$$S: c(x,t) \to I_k^{TH} = A \exp\left[-\varepsilon \frac{t_k}{\Delta t}\right] \int_{\mathbb{R}^2} d\tilde{x}g$$

$$(\tilde{x} - x_k, \mu^2) c(\tilde{x}, t_k) + I_{BG},$$
(16)

where the scaling parameter A can be set to 1 if the unit of intensity is arbitrary, the 2D point-spread function is given by

$$g(x,\mu^2) = \frac{1}{\sqrt{2\pi\mu^2}} \exp\left[-\frac{(x^{(1)})^2 + (x^{(2)})^2}{2\mu^2}\right],$$
 (17)

and I_{BG} is the background signal.

Inference in the case of pure diffusion without photobleaching

Here, we apply the inference method to the signal $\{Y_i^{DATA}\}_{i=1}^N$ in the case of a purely diffusive model when photobleaching during imaging is negligible, i.e., $\varepsilon=0$. In this case, the only kinetic parameter to infer is D, the diffusion coefficient. The analytical solution of diffusion PDE (1) with a generic initial condition c(y,0) can be expressed as

$$c(x,t) = \int_{\mathbb{R}^2} dy g(x - y, 2Dt) c(y,0)$$
 (18)

with g defined as in Eq. 17. If we apply the sampling operator S to c(x,t) and the compress the resulting vector $\{I_i^{TH}\}_{i=1}^N$, we obtain the theoretical compressed signal as

$$Y_{i}^{TH} = \sum_{k=0}^{N} \left\{ F_{i,k} \int_{\mathbb{R}^{2}} dy g(x_{k} - y, 2Dt_{k} + \mu^{2}) c(y, 0) + F_{i,k} I_{BG} \right\}$$
(19)

By comparison with Eq. 5, we identify the kernel matrix $G_i(x,y) = \sum_{g} g(x_k - y, 2Dt_k + \mu^2)$, the shift vector $h_i = 0$, and $w(y) = c(y, 0) + I_{\rm BG}^k$. We remark that in this case there is no need to estimate the background value to infer diffusion, as its contribution is incorporated into the initial perturbation w(y). Moreover, even if the width of the point-spread function μ is not known, in practice we can set this parameter equal to Δx , the pixel size. Indeed, we found that the average and the variance of the estimated parameter distribution are not affected by this choice as long as the true value of the system $\mu_{\rm true} \gtrapprox 1$ (see Fig. S4). We obtain the kernel matrix from Eq. 8 as

$$K_{i,j} = \sum_{k,l=0}^{N_{tot}} F_{i,k} F_{j,l} e^{-\frac{e}{\Delta t}(t_k + t_l)} g(x_k - x_l, 2D(t_k + t_l) + \mu^2),$$
(20)

from which it is possible to compute $\kappa^{(\ell)} = \sum_{k,l=0}^{N_{\rm tot}} \tilde{F}(q_i^{(\ell)}, x_k^{(\ell)}) \tilde{F}(q_j^{(\ell)}, x_l^{(\ell)}) e^{-e(t_k+t_l)/2} g(x_k^{(\ell)} - y_l^{(\ell)}, 2D(t_k+t_l) + \mu^2)$, with $\ell \in \{1, 2\}$, and U_R with Eq. 11. Finally, we infer the diffusion coefficient $D_{\rm est}$ by minimizing the cost function (Eq. 13).

Inference in the case of reaction-diffusion with photobleaching

Now we consider the underlying model to be a linear reaction-diffusion PDE (Eq. 2) and photobleaching during imaging not to be negligible, i.e., $\varepsilon \neq 0$. Following the same approach as in the previous section, the theoretical compressed signal takes the form

$$Y_{i}^{TH} = \sum_{k=1}^{N_{tot}} \left\{ F_{i,k} e^{-\frac{\epsilon}{\Delta t} I_{k}} \left(\left(\frac{\alpha}{\beta} - e^{-\beta t_{k}} \right) + e^{-\beta t_{k}} \int dy \, g \right) \right\}$$

$$\left(x_{k} - y, 2Dt_{k} + \mu^{2} \right) \left(c(y,0) - \alpha / \beta \right) + F_{i,k} I_{BG}$$

$$(21)$$

In this case, the set of parameters to *a priori* estimate from our method is listed in Table 4. By comparison with Eq. 5, we identify Y_i^{TH} and we obtain the kernel from Eq. 8

$$K_{i,j} = \sum_{i,j=1}^{N_{tot}} F_{i,k} F_{j,k} e^{-(\frac{\rho}{\Delta t} + \beta)(t_k + t_l)} g$$

$$(22)$$

$$(x_k - x_l, 2D(t_k + t_l) + \mu^2)$$

and

$$h_i(\alpha,\beta) = \sum_{k=1}^{N_{tot}} \left\{ F_{i,k} \alpha / \beta \left(1 - e^{-\beta t_i} \right) e^{-e^{\frac{t_i}{\Delta t}}} + F_{i,k} I_{BG} \right\}. \tag{23}$$

We note that $h_l(\alpha,\beta)$ is defined at $\beta=0$ by continuity using $\lim_{\beta\to 0}(1-\exp{(-\beta t_l)})/\beta=t_l$. From Eq. 22, we deduce $\kappa^{(\ell)}=\sum_{k,l=0}^{N_{\rm not}}\tilde{F}(q_i^{(\ell)},x_k^{(\ell)})\tilde{F}(q_j^{(\ell)},x_l^{(\ell)})e^{-\varepsilon+\beta)(t_k+t_l)/2}$ $g(x_k^{(\ell)}-y_l^{(\ell)},2D(t_k+t_l)+\mu^2)$, with $\ell\in\{1,2\}$, and U_R with Eq. 11. Finally, the cost function defined in Eq. 13 can be minimized with respect to the kinetic parameters D, α , β , and $I_{\rm BG}$. Since $I_{\rm BG}$ and α are linear parameters, the values, $I_{\rm min}^{\rm BG}$ and $\alpha_{\rm min}$, which minimize the cost for fixed D and β can be obtained analytically as

$$\begin{bmatrix} I_{\min}^{BG} \\ \alpha_{\min} \end{bmatrix} = \begin{bmatrix} \sum_{i=0}^{N} [J_{BG}]_{i}^{2} & \sum_{i=0}^{N} [J_{\alpha}]_{i} [J_{BG}]_{i} \\ \sum_{i=0}^{N} [J_{\alpha}]_{i} [J_{BG}]_{i} & \sum_{i=0}^{N} [J_{\alpha}]_{i}^{2} \end{bmatrix}^{-1}$$

$$\begin{bmatrix} \sum_{i=0}^{N} [J_{\alpha}]_{i}^{2} Y_{i}^{DATA} \sum_{i=0}^{N} [J_{\alpha}]_{i} Y_{i}^{DATA} \end{bmatrix}$$
(24)

where $[J_{\mathrm{BG}}]_i = \partial_{I_{\mathrm{BG}}} r_i$ and $[J_a]_i = \partial_{\alpha} r_i$ are the Jacobian of the residuals (7) with respect to I_{BG} and α taking the form

TABLE 4 Parameters of signal acquisition model and of PDE

I_{BG}	Background signal		
μ	width of point-spread function		
ϵ	rate of photobleaching during imaging		
D	diffusion coefficient		
α	source rate		
β	exchange (or dissociation) rate		

$$\begin{cases}
[J_{BG}]_{i} = \lambda \sum_{j=0}^{N} [K^{+}]_{i,j} \sum_{k=0}^{N_{\text{tot}}} F_{j,k} \\
[J_{\alpha}]_{i} = \lambda \sum_{j=0}^{N} [K^{+}]_{i,j} \sum_{k=0}^{N_{\text{tot}}} F_{j,k} \frac{\alpha}{\beta} (1 - e^{-\beta t_{k}}) e^{-\frac{\epsilon}{\Delta j} t_{k}}
\end{cases} (25)$$

So, the cost in Eq. 13 is computed directly at $I_{\rm BG} = I_{\rm min}^{BG}$ and $\alpha = \alpha_{\rm min}$ and minimized numerically with respect to D β , and ε , yielding the final estimations $D_{\rm est}$, $\beta_{\rm est}$, $\varepsilon_{\rm est}$, $I_{\rm est}^{BG} = I_{\rm min}^{BG}(D_{\rm est}, \beta_{\rm est}, \varepsilon_{\rm est})$, and $\alpha_{\rm est} = \alpha_{\rm min}(D_{\rm est}, \beta_{\rm est}, \varepsilon_{\rm est})$.

Improving parameters estimation using extrainformation

Even though we can estimate all parameters in Eq. 21, knowing a priori the background and the photobleaching decay rate can improve the estimation of model parameters $D_{\rm est}$, $\alpha_{\rm est}$, and $\beta_{\rm est}$. For this reason, it is important to take advantage of information available beyond the FRAPped area. A sample-free area gives access to the background I_{BG} by averaging the signal over this area. The photobleaching loss rate can be extracted from a region of the sample far enough from the FRAPped area, by an exponential fit \sim $e^{-\frac{\varepsilon}{\Delta t}t_i}$ to the spatial average signal over this area. Moreover, if a pre-FRAP image is present, we can obtain the stationary concentration c_s by averaging the signal over the area that is later FRAPped. This value sets the ratio between the exchange and source rate, $c_s = \alpha/\beta$. This a priori information can be integrated in the computation of the kernel and shift terms. In Table 5, we recapitulate the kernel and shift terms for all experimental conditions: with or without photobleaching, with or without an unfrapped control area, with or without a sample-free area, and with or without prebleaching images. It is important to remark that when photobleaching is absent and no background area is available, the contribution to the signal intensity of the source rate α and the background value I_{BG} cannot be distinguished. In such cases, HiFRAP can only estimate the combined parameter $\alpha^* = \alpha + \beta I_{BG}$. To determine α separately, the user must obtain the value of $I_{\rm BG}$ from independent experiments.

Numerical implementation

In this section, we describe the numerical implementation of HiFRAP using SciPy and NumPy package in Python. We wrapped the corresponding scripts in an ImageJ plugin also called HiFRAP.

We begin with the calculation of the cost function, which requires computing the inverse of a matrix $(K + \lambda Id)^{-1}$ (or its expression with U_R in Eq. 12). This is achieved using the Cholesky decomposition. Specifically, we first compute the Cholesky factor L using scipy.linalg.lapack.dpotrf. The inverse, L^{-1} , is then obtained using scipy.linalg.lapack.dtrtri, which takes advantage of the triangular shape of L using a recursive block algorithm. Finally, the pseudoinverse is given by $(K + \lambda Id)^{-1} = L^{-T}L^{-1}$. To obtain the threshold λ , the first eigenvalue is calculated by Lanczos bidiagonalization using scipy.linalg.svds.

To minimize the cost function (Eq. 13) with respect to D, β , and/or ε , we first determine an appropriate initial condition for these param-

eters to start from the numeric algorithm. In this context, we suppose the typical relaxation time of diffusion $t_D = \frac{e^2}{16D}$, dissociation rate $t_\beta = \log(2)/\beta$, and/or photobleaching $t_\varepsilon = \Delta t \log(2)/\varepsilon$ to be equal to half of the total observational window T. Since the typical bleaching size ℓ is not known, we approximate this value $\ell \approx L/2$, where L is the total spatial window. These yields as initial parameters $D_{\rm in} = (L/2)^2/16/T$ (or $(L/2)^2/8/T$ in 1D), $\beta_{in} = \log(2)/T$, and/or $\varepsilon_{in} = \frac{\log(2)\Delta t}{2}$.

Next, the full reflective trust region algorithm is applied as implemented in scipy.optimize.least_squares(method = 'trf'). Optimization is performed by restricting the parameter ranges according to the spatiotemporal observation window, as parameter values outside these ranges would be physically meaningless. For the diffusion coefficient D, we impose that the timescale associated with the slowest Fourier mode, of order L^2/D (where L denotes the total spatial window), must be larger than $5\Delta t$, ensuring sufficient temporal resolution. Conversely, the timescale associated with the fastest Fourier mode, of order $(L/n_q)^2/D$ (with n_q the highest wavenumber considered), must be smaller than 40T, where T denotes the total temporal observation time. For the exchange rate β , whose characteristic timescale is of order $1/\beta$, we constrain β such that $-T < 1/\beta < 100T$. Here, negative values of $1/\beta$ are allowed, as they can arise when the empirical error $\Delta \beta_{\rm emp}$ is comparable with the true value $\beta_{\rm true}$. For the photobleaching decay rate ε , we require that it is not negligible over the temporal window, restricting its values such that $100T < 1/\varepsilon < T/15$. During the optimization procedure, convergence is considered achieved when the relative variation in the estimated parameter vector $\vec{\theta}$ between successive iterations satisfies $\|\Delta \vec{\theta}/\vec{\theta}\| < 10^{-4}$.

Once the minimum of the cost function is found, the Hessian is computed using the Jacobian of residuals $r_i(\vec{\theta})$ divided by the square root of the trace $J_i = \nabla_{\vec{\theta}}(r_i(\vec{\theta})/\sqrt{N_{eff}(\vec{\theta})})$, using the approximation $H \approx \sum_{i=0}^N J_i \otimes J_i$, as implemented in the reflective trust region numerical method. The Jacobian is computed numerically by taking a finite step of the order of $10^{-2}\vec{\theta}_{\rm est}$, which corresponds to the typical noise error, except that the derivatives with respect to the source rate are computed analytically from Eq. 25. Finally, to evaluate the goodness of the fit, the null matrix Φ is obtained by computing the eigenvectors and eigenvalues of K or U_R using the SVD as implemented in numpy.linalg.svd.

Artificial data

Artificial concentration fields c(x,t) were obtained by solving analytically the reaction-diffusion Eq. 2 (or the diffusion Eq. 1), with known parameters D_{true} , α_{true} , and β_{true} . The initial condition describes a square FRAPped profile,

$$c(x, y, 0) = \begin{cases} c_s - \Delta c & \text{if} \quad |x - \frac{L}{2}| < \frac{\ell}{2} \text{ and } |y - \frac{L}{2}| < \frac{\ell}{2} \\ c_s & \text{else,} \end{cases}$$
(26)

where $\Delta c/c_{\rm s}$ is the proportion of bleached fluorophores and ℓ is the square side length. To get the signal vector, the concentration solution was multiplied by a factor A and convoluted with a Gaussian function of width $\mu_{\rm true}$ to mimic the effect of the point-spread function. Photobleaching during imaging is readily accounted for by multiplying the solution by an exponentially decaying function with rate $\varepsilon_{\rm true}$. The background value $I_{\rm true}^{\rm BG}$ was added to the resulting signal. The theoretical data vector takes the form

$$I_{k}^{DATA} = Ae^{-\frac{\epsilon_{\text{true}}}{\Delta I}t_{k}} \left(c_{\text{s}} - \Delta I e^{-\beta_{\text{true}}t_{k}} \frac{1}{2} \psi \left(x_{k}^{(1)} \right) \psi \left(x_{k}^{(2)} \right) \right) + I_{\text{true}}^{\text{BG}},$$
(27)

TABLE 5 Summary of the kernel and shift term formulas for each model under different experimental conditions

Model	Prebl.	Photobl.	Back.	Kernel	Shift term
D	yes/no	no	yes/no	$g(x_k - x_l, 2D(t_k + t_l) + \mu^2)$	1
D	yes/no	yes	yes/no	$e^{-\frac{\varepsilon}{\Delta t}(t_k+t_l)}g(x_k-x_l,2D(t_k+t_l)+\mu^2)$	$I_{ m BG}$
RD/R	yes	no	no	$e^{-\beta(t_k+t_l)}g(x_k - x_l, 2D(t_k+t_l) + \mu^2)$	$I_{ m tot}$
RD/R	yes	yes	no	$e^{-\beta(t_k+t_l)}g(x_k - x_l, 2D(t_k+t_l) + \mu^2)$	$I_{\text{tot}}e^{-t_k}\frac{\varepsilon}{\Delta t} + I_{\text{BG}}(1 - e^{-t_k}\frac{\varepsilon}{\Delta t})$
RD/R	yes	yes/no	yes	$e^{-\left(\beta+\frac{\mathcal{E}}{\Delta t}\right)\left(t_k+t_l\right)}g(x_k-x_l,2D(t_k+t_l)+\mu^2)$	$c_s e^{-t_k \frac{\varepsilon}{\Delta t}} + I_{BG}$
RD/R	no	no	no	$e^{-\beta(t_k+t_l)}g(x_k - x_l, 2D(t_k+t_l) + \mu^2)$	$\alpha^*/\beta(1 - e^{-\beta t_k})$
RD/R	no	no	yes	$e^{-\beta(t_k+t_l)}g(x_k - x_l, 2D(t_k+t_l) + \mu^2)$	$\alpha/\beta(1 - e^{-\beta t_k}) + I_{\mathrm{BG}}$
RD/R	no	yes	yes/no	$e^{-\left(\beta+\frac{\varepsilon}{\Delta t}\right)\left(t_k+t_l\right)}g(x_k-x_l,2D(t_k+t_l)+\mu^2)$	$\alpha/\beta(1 - e^{-\beta I_k})e^{-\frac{\varepsilon}{\Delta t}t_k} + I_{\mathrm{BG}}$

From left to right: model (diffusion, D; reaction, R; or reaction-diffusion, RD), presence of prebleaching images (yes or no), whether imaging induces photobleaching (yes or no), whether a sample-free background area is available (yes or no), and corresponding kernel and shift term (without compression for ease of notation). The diffusion coefficient, D, and exchange rate, β , are always estimated by numerical minimization of the cost function or set to zero in the formulas when not included in the model. The background signal, I_{BG} , is estimated by averaging the signal in the background area when this information is available; otherwise, if I_B appears in the formula, its estimated value is determined through analytical minimization of the cost function. The stationary concentration (in arbitrary units), c_s , is estimated by averaging the prebleaching images and subtracting the background I_{BG} when both prebleaching and background areas exist. When the background does not exist, the average prebleaching signal corresponds to I_{tot} , the sum of the background signal and the stationary concentration. The source rate, α , is determined via analytical minimization of the cost function or a posteriori as $\alpha_{est} = c_s/\beta_{est}$ when c_s is known, or as $\alpha_{est} = (I_{tot} - I_{BG})/\beta_{est}$ when the background is estimated through cost minimization. In the other cases (third and sixth rows), it is not possible to estimate directly α but only the parameter $\alpha^* = \alpha + \beta I_{BG}$ from analytical minimization of the cost function (sixth row) or a posteriori from $\alpha^*_{est} = I_{tot}\beta_{est}$ if I_{tot} is known (third row). The photobleaching decay rate ε is either computed from the control area when present or by numerical minimization of the cost function. Δt is the time interval between two images while the function g is defined in Eq. 17.

with

$$\psi\left(x_{k}^{(p)}\right) = \operatorname{erf}\left(\frac{x_{k}^{(p)} - \frac{\ell}{2}}{\sqrt{4D_{\operatorname{true}}t_{k} + 2\mu_{\operatorname{true}}^{2}}}\right)$$
$$- \operatorname{erf}\left(\frac{x_{k}^{(p)} + \frac{\ell}{2}}{\sqrt{4D_{\operatorname{true}}t_{k} + 2\mu_{\operatorname{true}}^{2}}}\right),$$

where the error function is defined as $\operatorname{erf}(x^{(p)}) = \frac{2}{\sqrt{\pi}} \int_0^{x^{(p)}} e^{-l^2} dt$ and $\Delta I = A\Delta c$ the signal drop-off. The stationary concentration c_s is fixed for pure diffusion, whereas for reaction-diffusion, $c_s = \alpha_{\operatorname{true}}/\beta_{\operatorname{true}}$. The same procedure was applied for a Gaussian bleaching profile, X shape, and E shape (obtained by translation, rotation, extension, and superposition of square bleaching profile).

To obtain a realistic data set we add noise to the deterministic solution,

$$I_k^{DATA} = I_k^{TH} + \eta \mathcal{N}_k, \tag{28}$$

where η is noise amplitude and \mathcal{N}_k is sampled from a Gaussian random variable of mean zero and standard deviation 1. Finally, we compress the simulated vector (Eq. 27) using the compression operator \mathcal{C} (Eq. 3).

Unless specified otherwise, we used the following default values: $n_x=121,\ n_t=16,\ \ell/(n_x\Delta x)=3,\ \mu_{\rm true}/\Delta x=1,\ \eta/\Delta I=0.25,\ I_{\rm BG}/\Delta I=0.5,\ c_s/\Delta I=2$ with $\Delta x=1,\ \Delta t=1,\ \Delta I,\ A=1$ in arbitrary units; for diffusive systems $D_{\rm true}=2\ell^2/16/(n_t-1)/\Delta t$ or $D_{\rm true}=7\ell^2/16/\Delta t/(n_t-1)$ (if photobleaching is present) and $\beta_{\rm true}=0$; for reaction-diffusive systems $D_{\rm true}=7/2\ell^2/16/(n_t-1)/\Delta t,\ \alpha_{\rm true}=\beta_{\rm true}c_s,\ \beta_{\rm true}=7/2\log(2)/(n_t-1)/\Delta t;$ if photobleaching is present $\varepsilon_{\rm true}=1/(n_t-1)$ otherwise $\varepsilon_{\rm true}=0$.

Experiments

The Schizosaccharomyces pombe strain mtl2-GFP:ura4+ (identifier RN21 (12)) was used for experimental validation of the method. Standard fission yeast methods and media were used (64). The cells were grown in YE5S liquid culture overnight at 25°C, diluted in fresh medium and grown to an optical density (OD_{600}) between 0.4 and 0.6 before live-imaging. Cells were imaged on EMM (minimal medium) 2% agarose pads at room temperature (22-25°C); EMM shows reduced background noise in comparison with YE5S agarose pads. Cells were imaged at their bottom surface, close to the coverslip. Images were acquired with a 100× oil-immersion objective (CFI Plan Apo DM $100\times/1.4$ NA, Nikon, Minato City, Tokyo, Japan) on an inverted spinning-disk confocal microscope equipped with a motorized stage and an automatic focus (Ti-Eclipse, Nikon, Minato City, Tokyo, Japan), a Yokogawa (Musashino, Tokyo, Japan) CSUX1FW spinning unit, a Prime BSI camera (Teledyne Photometrics, Tucson, Arizona) and an iLas2 module (GATACA Systems, Massy, France) for FRAP. During FRAP, a 0.4 μ m square ROI was bleached with the 491 nm laser at 20-60% power and 30 repetitions and the fluorescence recovery was monitored for a time interval ranging from 7-10 s.

An online supplement to this article can be found by visiting *BJ Online* at http://www.biophysj.org.

ACKNOWLEDGMENTS

This work was funded by Agence Nationale de la Recherche (project CellWallSense, ANR-20-CE130003-01 to N.M. and A.B.).

AUTHOR CONTRIBUTIONS

E.L. designed and implemented the theory. C.M.-D. performed the experiments. N.M. supervised the experiments. A.B. and A.F. designed and supervised the study.

DECLARATION OF INTERESTS

The authors declare no competing interests.

SUPPORTING MATERIAL

Supporting material can be found online at https://doi.org/10.1016/j.bpj. 2025.07.036.

REFERENCES

- Chen, Y., B. C. Lagerholm, ..., K. Jacobson. 2006. Methods to measure the lateral diffusion of membrane lipids and proteins. *Methods*. 39:147–153.
- Jacobson, K., A. Ishihara, and R. Inman. 1987. Lateral diffusion of proteins in membranes. *Annu. Rev. Physiol.* 49:163–175.
- Lorén, N., J. Hagman, ..., K. Braeckmans. 2015. Fluorescence recovery after photobleaching in material and life sciences: putting theory into practice. Q. Rev. Biophys. 48:323–387.
- Reits, E. A., and J. J. Neefjes. 2001. From fixed to FRAP: measuring protein mobility and activity in living cells. *Nat. Cell Biol.* 3:E145– E147. https://www.nature.com/articles/ncb0601_e145.
- Ishikawa-Ankerhold, H., R. Ankerhold, and G. Drummen. 2014. Fluorescence Recovery After Photobleaching (FRAP). In eLS. John Wiley & Sons. Ltd. Chichester.
- Goehring, N. W., D. Chowdhury, ..., S. W. Grill. 2010. FRAP Analysis
 of Membrane-Associated Proteins: Lateral Diffusion and MembraneCytoplasmic Exchange. *Biophys. J.* 99:2443–2452. https://www.ncbi.
 nlm.nih.gov/pmc/articles/PMC2956213/.
- van Royen, M. E., P. Farla, ..., A. B. Houtsmuller. 2008. Fluorescence recovery after photobleaching (FRAP) to study nuclear protein dynamics in living cells. *Nucleus (Karachi)*. 2:363–385, Chromatin, Transcription, Envelope, Proteins, Dynamics, and Imaging.
- Dundr, M., U. Hoffmann-Rohrer, ..., T. Misteli. 2002. A kinetic framework for a mammalian RNA polymerase in vivo. *Science*. 298:1623–1626.
- Bläßle, A., G. Soh, ..., P. Müller. 2018. Quantitative diffusion measurements using the open-source software PyFRAP. Nat. Commun. 9:1582, number: 1 Publisher: Nature Publishing Group. https://www.nature.com/articles/s41467-018-03975-6.
- Kourtis, N., and N. Tavernarakis. 2017. Protein synthesis rate assessment by fluorescence recovery after photobleaching (FRAP). Bio. Protoc. 7:e2156.
- Taylor, N. O., M.-T. Wei, ..., C. P. Brangwynne. 2019. Quantifying dynamics in phase-separated condensates using fluorescence recovery after photobleaching. *Biophys. J.* 117:1285–1300.
- Neeli-Venkata, R., C. M. Diaz, ..., N. Minc. 2021. Detection of surface forces by the cell-wall mechanosensor Wsc1 in yeast. *Dev. Cell*. 56:2856–2870.e7. https://www.sciencedirect.com/science/article/pii/ S1534580721007681.
- Ciocanel, M.-V., J. A. Kreiling, ..., B. Sandstede. 2017. Analysis of active transport by fluorescence recovery after photobleaching. *Biophys. J.* 112:1714–1725.
- Erami, Z., D. Herrmann, ..., P. Timpson. 2016. Intravital FRAP imaging using an E-cadherin-GFP mouse reveals disease- and drug-dependent dynamic regulation of cell-cell junctions in live tissue. *Cell Rep.* 14:152–167.
- Hardin, J. 2011. Chapter 14 Imaging Embryonic Morphogenesis in C. elegans. In Caenorhabditis elegans: Molecular Genetics and Development, Academic Press, Volume 106 of Methods in Cell Biology.
 J. H. Rothman and A. Singson, eds Elsevier, pp. 377–412. https://www.sciencedirect.com/science/article/pii/B9780125441728000141.
- Recouvreux, P., P. Pai, ..., P.-F. Lenne. 2024. Transfer of polarity information via diffusion of Wnt ligands in C. elegans embryos. *Curr. Biol.* 34:1853–1865.e6.

- Lamiré, L.-A., P. Milani, ..., M. Grammont. 2020. Gradient in cytoplasmic pressure in germline cells controls overlying epithelial cell morphogenesis. *PLoS Biol.* 18:1–30. https://doi.org/10.1371/journal. pbio.3000940.
- Deschout, H., K. Raemdonck, ..., K. Braeckmans. 2014. FRAP in pharmaceutical research: practical guidelines and applications in drug delivery. *Pharm. Res.* 31:255–270.
- Axelrod, D., D. E. Koppel, ..., W. W. Webb. 1976. Mobility measurement by analysis of fluorescence photobleaching recovery kinetics. *Biophys. J.* 16:1055–1069.
- Kang, M., C. A. Day, ..., E. DiBenedetto. 2012. Simplified equation to extract diffusion coefficients from confocal FRAP data. *Traffic*. 13:1589– 1600. https://www.ncbi.nlm.nih.gov/pmc/articles/PMC3731631/.
- Elowitz, M. B., M. G. Surette, ..., S. Leibler. 1999. Protein Mobility in the Cytoplasm of Escherichia coli. *J. Bacteriol.* 181:197–203. https:// www.ncbi.nlm.nih.gov/pmc/articles/PMC103549/.
- Zarabadi, A. S., and J. Pawliszyn. 2015. Accurate determination of the diffusion coefficient of proteins by Fourier analysis with whole column imaging detection. *Anal. Chem.* 87:2100–2106.
- Jönsson, P., M. P. Jonsson, ..., F. Höök. 2008. A method improving the accuracy of fluorescence recovery after photobleaching analysis. *Biophys. J.* 95:5334–5348.
- Berk, D. A., F. Yuan, ..., R. K. Jain. 1993. Fluorescence photobleaching with spatial Fourier analysis: measurement of diffusion in light-scattering media. *Biophys. J.* 65:2428–2436. https://www.sciencedirect. com/science/article/pii/S0006349593813262.
- Deschout, H., J. Hagman, ..., K. Braeckmans. 2010. Straightforward FRAP for quantitative diffusion measurements with a laser scanning microscope. Opt. Express. 18:22886–22905.
- Papáček, Š., R. Kaňa, and C. Matonoha. 2013. Estimation of diffusivity of phycobilisomes on thylakoid membrane based on spatio-temporal FRAP images. *Math. Comput. Model.* 57:1907–1912.
- Blumenthal, D., L. Goldstien, ..., L. A. Gheber. 2015. Universal Approach to FRAP Analysis of Arbitrary Bleaching Patterns. Sci. Rep. 5:11655.
- Klaus, C. J. S., K. Raghunathan, ..., A. K. Kenworthy. 2016. Analysis
 of diffusion in curved surfaces and its application to tubular membranes. Mol. Biol. Cell. 27:3937–3946.
- **29.** Geiger, A. C., C. J. Smith, ..., G. J. Simpson. 2020. Anomalous diffusion characterization by Fourier transform-FRAP with patterned illumination. *Biophys. J.* 119:737–748.
- Yuste, S. B., E. Abad, and K. Lindenberg. 2014. A reaction– subdiffusion model of fluorescence recovery after photobleaching (FRAP). J. Stat. Mech. 2014:P11014.
- Lele, T., S. R. Wagner, ..., D. E. Ingber. 2006. Methods for measuring rates of protein binding to insoluble scaffolds in living cells: Histone H1-chromatin interactions. *J. Cell. Biochem.* 99:1334–1342. https:// onlinelibrary.wiley.com/doi/abs/10.1002/jcb.20997.
- McNally, J. G. 2008. Quantitative FRAP in analysis of molecular binding dynamics in vivo. *Methods Cell Biol.* 85:329–351.
- Tsibidis, G. D. 2009. Quantitative interpretation of binding reactions of rapidly diffusing species using fluorescence recovery after photobleaching. J. Microsc. 233:384–390.
- 34. Mueller, F., D. Mazza, ..., J. G. McNally. 2010. FRAP and kinetic modeling in the analysis of nuclear protein dynamics: what do we really know? *Curr. Opin. Cell Biol.* 22:403–411.
- Sprague, B. L., and J. G. McNally. 2005. FRAP analysis of binding: proper and fitting. *Trends Cell Biol*. 15:84–91. https://www.sciencedirect.com/science/article/pii/S0962892404003332.
- Cowan, A. E., and L. M. Loew. 2023. Beyond analytic solution: Analysis of FRAP experiments by spatial simulation of the forward problem. *Biophys. J.* 122:3722–3737.
- 37. Kang, M., and A. K. Kenworthy. 2008. A closed-form analytic expression for FRAP formula for the binding diffusion model. *Biophys. J.* 95: L13–L15.

- 38. Kang, M., C. A. Day, ..., A. K. Kenworthy. 2010. A quantitative approach to analyze binding diffusion kinetics by confocal FRAP. Biophys. J. 99:2737-2747.
- 39. Ciocanel, M.-V., L. Ding, ..., B. Sandstede. 2024. Parameter Identifiability in PDE Models of Fluorescence Recovery After Photobleaching. Bull. Math. Biol. 86:36. https://doi.org/10.1007/s11538-024-01266-4
- 40. Wu, J., Y. Fang, ..., C. Zhu. 2008. A coupled diffusion-kinetics model for analysis of contact-area FRAP experiment. Biophys. J. 95:910-919.
- 41. Tolentino, T. P., J. Wu, ..., C. Zhu. 2008. Measuring diffusion and binding kinetics by contact area FRAP. Biophys. J. 95:920-930.
- 42. Röding, M., L. Lacroix, ..., N. Lorén. 2019. A highly accurate pixelbased FRAP model based on spectral-domain numerical methods. Biophys. J. 116:1348-1361.
- 43. Montero Llopis, P., O. Sliusarenko, ..., C. Jacobs-Wagner. 2012. In vivo biochemistry in bacterial cells using FRAP: insight into the translation cycle. Biophys. J. 103:1848-1859.
- 44. Berkovich, R., H. Wolfenson, ..., M. Urbakh. 2011. Accurate Quantification of Diffusion and Binding Kinetics of Non-integral Membrane Proteins by FRAP. Traffic. 12:1648-1657.
- 45. Saito, T., D. Matsunaga, and S. Deguchi. 2022. Long-term molecular turnover of actin stress fibers revealed by advection-reaction analysis in fluorescence recovery after photobleaching. PLoS One. 17: e0276909.
- 46. Cruz, S., S. Muñoz, ..., Y. Sanchez. 2013. The fission yeast cell wall stress sensor-like proteins Mtl2 and Wsc1 act by turning on the GTP ase Rho1p but act independently of the cell wall integrity pathway. Microbiology. 2:778-794.
- 47. Branch, M. A., T. F. Coleman, and Y. Li. 1999. A subspace, interior, and conjugate gradient method for large-scale bound-constrained minimization problems. SIAM J. Sci. Comput. 21:1-23.
- 48. Berger, V. W., and Y. Zhou. 2014. Kolmogorov-smirnov Test: Overview. Wiley statsref: Statistics reference online.
- 49. Bianchi, F., Ł. Syga, ..., B. Poolman. 2018. Steric exclusion and protein conformation determine the localization of plasma membrane transporters. Nat. Commun. 9:501.
- 50. Ganguly, S., P. Singh, ..., A. Chattopadhyay. 2009. Differential dynamics of membrane proteins in yeast. Biochem. Biophys. Res. Commun. 387:661-665.
- 51. Ries, J., C. Klose, ..., P. Schwille. 2008. How to measure slow diffusion in yeast cell membranes. . Biophotonics: Photonic Solutions for Better

- Health Care, 6991. SPIE, pp. 136–143. https://www.spiedigitallibrary. org/conference-proceedings-of-spie/6991/69910W/How-to-measureslow-diffusion-in-yeast-cell-membranes/10.1117/12.787043.full.
- 52. Valdez-Taubas, J., and H. R. B. Pelham. 2003. Slow diffusion of proteins in the yeast plasma membrane allows polarity to be maintained by endocytic cycling. Curr. Biol. 13:1636–1640.
- 53. Martinière, A., I. Lavagi, ..., J. Runions. 2012. Cell wall constrains lateral diffusion of plant plasma-membrane proteins. Proc. Natl. Acad. Sci. USA. 109:12805–12810. https://app.readcube.com/library/ 66e6a98f-7942-43f4-ae85-decb5da751eb/item/5c9445c0-a3e3-4a6bae89-4722aaa12fb6.
- 54. Wieser, S., J. Weghuber, ..., G. J. Schütz. 2009. Cell-to-cell variability in the diffusion constants of the plasma membrane proteins CD59 and CD147. Soft Matter. 5:3287.
- 55. Hillsley, A., J. Stein, ..., J. Funke. 2024. A Bayesian Solution to Count the Number of Molecules within a Diffraction Limited Spot. Preprint at bioRxiv. https://www.biorxiv.org/content/early/2024/04/22/2024.04.18. 590066.
- 56. Liu, Z., T. Lemma, and J. Pawliszyn. 2006. Capillary isoelectric focusing coupled with dynamic imaging detection: A one-dimensional separation for two-dimensional protein characterization. J. Proteome Res. 5:1246-1251.
- 57. Ferenczi, E. A., X. Tan, and C. L.-H. Huang. 2019. Principles of optogenetic methods and their application to cardiac experimental systems. Front. Physiol. 10:1096.
- 58. Karnakov, P., S. Litvinov, and P. Koumoutsakos. 2024. Solving inverse problems in physics by optimizing a discrete loss: Fast and accurate learning without neural networks. PNAS Nexus. 3:gae005.
- 59. Milton, P., H. Coupland, ..., S. Bhatt. 2019. Spatial analysis made easy with linear regression and kernels. *Epidemics*. 29:100362.
- 60. Press, W. H., S. A. Teukolsky, ..., B. P. Flannery. 2007. Numerical Recipes. Cambridge University Press.
- 61. Aggarwal, C. C. 2020. Linear Algebra and Optimization for Machine Learning. Springer.
- 62. Wahba, G. 1990. Spline Models for Observational Data. SIAM.
- 63. Emerson, R. W. 2020. Regression Analysis and Adjusted R2. J. Vis. Impair. Blind. (JVIB). 114:332-334.
- 64. Forsburg, S. L., and N. Rhind. 2006. Basic methods for fission yeast. Yeast. 23:173-183.